AFOSR-TR- 92 0250

DAMAGE ACCUMULATION PROCESS IN ADVANCED METAL MATRIX COMPOSITE UNDER THERMAL CYCLING

Minoru Taya
William D. Armstrong
Marty Dunn
Department of Mechanical Engineering
University of Washington
Seattle, Washington 98195

AFOSR Technical Report (AFOSR-91-0234)
covering October 1, 1990 through September 20, 1991

December 1991

unclassified
SECURITY CLASSIFICATION OF THIS PAGE

REPORT DOCUMENTATION PAGE

Form Approved OMB No. 0704-0188

1a. REPORT SECURITY CLASSIFICATION: unclassified	1b. RESTRICTIVE MARKINGS
2a. SECURITY CLASSIFICATION AUTHORITY	3. DISTRIBUTION/AVAILABILITY OF REPORT: Unlimited
2b. DECLASSIFICATION/DOWNGRADING SCHEDULE	
4. PERFORMING ORGANIZATION REPORT NUMBER(S): UW-ME-91-002	5. MONITORING ORGANIZATION REPORT NUMBER(S)
6a. NAME OF PERFORMING ORGANIZATION: University of Washington; 6b. OFFICE SYMBOL (If applicable): UW-ME	7a. NAME OF MONITORING ORGANIZATION: Air Force Office of Scientific Research ATTN. Dr. Walter F. Jones
6c. ADDRESS (City, State, and ZIP Code): Dept. of Mechanical Engineering, FU-10 Seattle, WA 98195	7b. ADDRESS (City, State, and ZIP Code): Bolling Air Force Base Washington, D.C. 200332
8a. NAME OF FUNDING/SPONSORING ORGANIZATION: Air Force Office of Sci. Res; 8b. OFFICE SYMBOL (If applicable): AFOSR /NA	9. PROCUREMENT INSTRUMENT IDENTIFICATION NUMBER: AFOSR-91-0234
8c. ADDRESS (City, State, and ZIP Code): Bolling Air Force Base Washington, D.C. 20332	10. SOURCE OF FUNDING NUMBERS: PROGRAM ELEMENT NO. 61102F; PROJECT NO. 2302; TASK NO. BS; WORK UNIT ACCESSION NO.

11. TITLE (Include Security Classification): Damage Accumulation Process in Advanced Metal Matrix Composite Under Thermal Cycling (u)

12. PERSONAL AUTHOR(S): Minoru Taya, William D. Armstrong, Marty Dunn

13a. TYPE OF REPORT	13b. TIME COVERED	14. DATE OF REPORT (Year, Month, Day)	15. PAGE COUNT
Final Report	FROM 10/16/90 TO 11/15/91	Nov. 20, 1991	

16. SUPPLEMENTARY NOTATION

17. COSATI CODES			18. SUBJECT TERMS (Continue on reverse if necessary and identify by block number)
FIELD	GROUP	SUB-GROUP	Damage Accumulation in Thermal-Cycled Metal Matrix Composites: Experimental and Analytical Studies.

19. ABSTRACT (Continue on reverse if necessary and identify by block number)

This research was intended to document the second stage of thermal cycling damage in metal matrix composites where progressive dimensional change along the fiber is observed. This dimensional change was documented by SEM-image analysis technique in terms of damage area distribution along the matrix-fiber interface. The progressive dimensional change was then predicted by using elastic/plastic/creep analytical model, resulting in a good agreement. Based on the analytical study, we designed a new type of MMC which possesses higher thermal cycling resistance and where additional short fibers are embedded in the matrix to make a MMC hybrid MMC. It was found that the main mechanisms for higher thermal cycling resistance in the hybrid MMC are:

(1) The apparent CTE of the matrix modified with additional short fibers is closer to that of the main fibers, resulting in smaller CTE mismatch, which would be a weaker driving force for thermal cycling damage.

(over)

20. DISTRIBUTION/AVAILABILITY OF ABSTRACT	21. ABSTRACT SECURITY CLASSIFICATION
☒ UNCLASSIFIED/UNLIMITED ☒ SAME AS RPT. ☐ DTIC USERS	unclassified

22a. NAME OF RESPONSIBLE INDIVIDUAL	22b. TELEPHONE (Include Area Code)	22c. OFFICE SYMBOL
Walter F. Jones	202-767-4987	AFOSR

DD Form 1473, JUN 86 — Previous editions are obsolete.

19. Abstract (cont.)

(2) Additional short fibers in the matrix give rise to higher density of dislocations which are punched out from the interface between the matrix and these short fibers, enhancing the in-situ mechanical properties of the matrix.

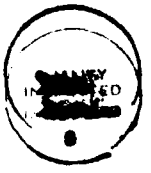

Table of Contents

1. INTRODUCTION

Metal matrix composites (MMCs) have been sought as a strong candidate for high performance structural materials for use in both room and high temperature environments. The thermo-mechanical behavior of various types of MMCs has recently been reviewed.[1] Although the mechanical behavior of MMCs in room temperature use environments was superior to that of the unreinforced metal, it is the high temperature use environment in which degradation in the mechanical behavior of the MMCs has been recognized. Typical high temperature use environments that MMCs experience are creep and thermal cycling. Normally the creep rate of a MMC is much less than that of the unreinforced metal, thus exhibiting the merit of reinforcing the metal by fibers. In the long term, although the interface of the matrix and fiber may become degraded due to diffusion of matrix metal and fiber materials. It is, however, thermal cycling that often limits the use of otherwise promising MMCs in high temperature applications. Degradation of the mechanical properties and dimensional instability of MMCs subjected to thermal cycling have been reported.[2–15] Table 1 shows a summary of the degradation modes of various types of MMCs reported so far in the literature.[16] The degradation modes stated in Table 1 stem from the mismatch in the coefficient of thermal expansion (CTE) of the matrix metal and fiber (normally made of refractory metal or ceramics). The CTE mismatch strain is equal to $(\alpha_f-\alpha_m)\Delta T$ where α_f and α_m are CTE of the fiber and matrix metal, and ΔT is the temperature difference undergone by the MMC. This CTE mismatch strain induces an internal stress field with its maximum in and around a fiber, resulting in the yielding of the matrix if its magnitude is large. Under thermal cycling, this internal stress field and cyclic plastic straining of the matrix metal with alternative sign is equivalent to low cycle (mechanical) fatigue described by Manson[17]. This thermal cycling fatique results in the microdamage of the matrix-fiber interface: voids in W/Cu composite[7], cracks in B/6061 Al composite[4], and also macrodamage such as dimensional changes, which are unacceptable since MMC components undergoing such dimensional changes may not function properly in a use environment.

Table 1. A Summary of Previously Reported Thermal Cycling Damage of MMCs

MMC Systems	Thermal Cycling Conditions	Degradation Modes	References
B/1100, 2024 and 6061 Al	T_{min} = RT T_{max} = 315, 365, N = 6000	surface roughening. internal notching of one matrix	(2)
B/6061 Al	T_{min} = RT T_{max} = 455°C N = 1000, 2059, and	cracking in the interfacial brittle zone	(4)
B/1100, 6061 Al	T_{min} = 50°C T_{max} = 320, 420°C	reaction product. AlB_2 caused flawed B fibers	(5)
α-Al_2O_3 (FP)/Al-Li	T_{min} = 140°C T_{max} = 500°C N = 205, 1440, 2830	voids at the reaction product $Li_2O \cdot 5Al_2O_3$	(8)
α-Al_2O_3(FP)/ EZ 33 Mg	T_{min} = 50°C T_{max} = 250,350°C N = up to 3000	voids at the interface, matrix cracking, matrix softening	(11)
Carbon (M40)/ 5056 Al	T_{min} = RT T_{max} = 250~400°C N = 10~1000	debonding at the interface	(13)
SiC_w/2024 Al	T_{min} = RT T_{max} = 400,500°C N = 100,1000	dimensional change in three-directions	(12)
W/Cu	T_{min} = 200,400°C T_{max} = 800°C N = up to 4950	sliding at the interface	(6)
W/Cu	T_{min} = 200°C T_{max} = 800°C N = 200	voids at the interface	(7)
W-1%ThO_2/ FeCrAlY	T_{min} = 29°C T_{max} = 1204°C N = 1000	surface roughening	(3), (15)
Mo-TZM/FeCrAlY	T_{min} = 29°C T_{max} = 1093,1204°C N = 100,1000	surface cracking, recrystallization of TZM	(3)
W/superalloys	T_{min} = RT T_{max} = up to 1100°C	cracking at the interface	(9)
W-2wt%ThO_2/ stainless steel Kovar, Inconel 718, Hastelloy X	T_{min} = 90°C T_{max} = 925°C N = up to 3600	cracking and debonding of the interface	(16)
W/FeCrAlY	T_{min} = RT T_{max} = 850,1000, 1090°C	voids in the matrix	(14)
W-1% ThO_2/ FeCrAlY	T_{min} = RT T_{max} = 1100°C	cracks in interface	(19)

In this report, an attempt is made to study experimentally and analytically the mechanisms of dimensional changes of thermally-cycled MMCs. To this end, we have chosen as a target MMC a W-ThO_2 fiber/FeCrAlY matrix (W/FeCrAlY) composite. The experimental study of the W/FeCrAlY composite will be discussed in Section 2. Analytical modeling of dimensional change will be summarized in Section 3. A comparison will then be made between the present experimental results and the predictions based on the proposed analytical model in Section 4. The conclusion is given in Section 5.

2. EXPERIMENT

2.1 MMC Specimens

In this study, we have used four different types of W/FeCrAlY composites: aligned continuous fiber MMC (CF), aligned short fiber MMC of fiber aspect ratio 5 (ASF-5) and 20 (ASF-20), and a hybrid MMC (AF). In the hybrid MMC, chopped Al_2O_3 fibers are combined with the FeCrAlY metal matrix of the ASF-20 composite with the intention of modifying the otherwise large CTE mismatch strain that would exist between the W fiber and FeCrAlY matrix. These MMC types are summarized in Table 2.

Table 2. MMC types used

MMC Type	Name	Vol. Frac. of W fiber (%)	Vol. Frac. of Al_2O_3 fibers(%)
aligned continuous fiber MMC	CF	31.9	0
aligned short fiber MMC (aspect ratio=5)	ASF-5	19.4	0
aligned short fiber MMC (aspect ratio=20)	ASF-20	19.5	0
hybrid MMC	AF	18.4	10.0

Processing of the MMC specimens are stated in subsection 2.1, and thermal cycling testing is described in subsection 2.2. Finally the results of the thermal cycling tests are presented in subsection 2.3.

2.2 Processing of MMC Specimens

The processing route of the MMC specimens involves several steps: processing of a matrix mat through tape casting, processing of fiber mats (different for the case of continuous fibers, and short fibers), burn-off of polymer binders, consolidation by hot isostatic press (HIP), and machining into specimens. The processing route is illustrated schematically in Fig. 1. The matrix metal FeCrAlY was supplied by General Electric Corp. in powder form with a nominal diameter of 15 μm. The W-ThO_2 fibers were supplied by General Electric in a wire form of nominal diameter of 250 μm, while Al_2O_3 fibers (FP trade name) were supplied by DuPont and their nominal diameter is 19 μm.

In the case of a continuous fiber MMC, fiber mats are cut from wound fiber sheets prepared by filament winding where a polymer binder was used. A similar procedure was utilized for producing the short fiber MMCs, although alignment of the short fiber mats required additional care.

The polymer burn-off operation is necessary to remove the various polymer materials used in making composite preforms. The most desirable process is the diffusion and reaction of atmospheric oxygen with polymer materials producing CO_2 and H_2O gaseous reaction products, while minimizing the oxidation of the metal powder. After a trial and error process, we found that the best burn-off schedule consists of a rapid temperature climb to 200°C followed by a slow two hour ramp to 300°C. The temperature was held at 300°C for two hours followed by ramp from 300°C to 350°C for two hours. Finally the preform was cooled-down to room temperature. The entire burn-off procedure required approximately nine hours.

The HIP process used required the temperature and pressure to be increased to 1150°C and 1500 MPa, respectively in two hours. Both conditions were then held for two hours, followed by a rapid release in pressure and slow cool in temperature over night so as to allow creep and diffusional relaxation processes to relax the internal stresses in the MMC.

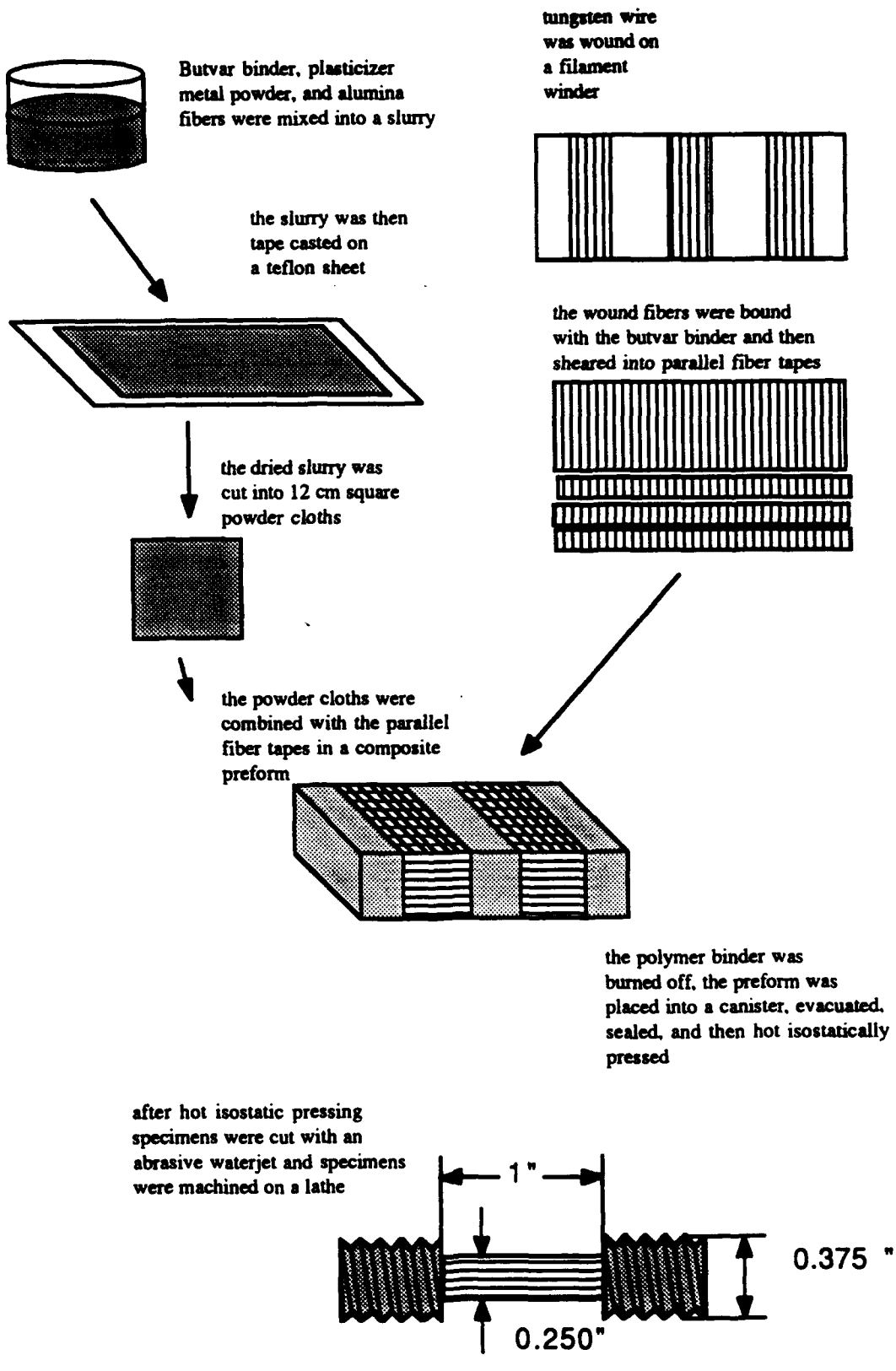

Figure 1. Schematic Diagram of the Composite Processing and Fabrication Process.

MMC specimens are so hard conventional machining methods are impossible to apply because they are too time consuming. We thus employed abrasive waterjet cutting method to rough machine the HIP bulk specimen into rod shapes followed by precision machining by tungsten carbide cutting tools. If W-ThO_2 fibers become exposed to the atmosphere due to machining, faster oxidation of the MMC specimen results. To avoid this, a thermal spray of metal FeCrALY powder was applied to the surface of the MMC specimens, with the thickness of coating being nominally 0.2 mm. Further details of the MMC processing have been given in our previous report.[18]

2.3 Thermal Cycling Testing and Dimensional Changes

The apparatus for thermal cycling testing (hereafter thermal cycler) is shown in Fig. 2 indicating two furnaces. Each furnace is a fluidized bed so as to ensure rapid heat transfer to a MMC specimen. The specimen shuttles within 10 seconds between the low temperature (T_{min}) and high temperature (T_{max}) furnaces with programmed time sequence controlled by a DC motor time switch. T_{max} can be as high as 1400°C while T_{min} can be reduced to room temperature. Examples of a typical temperature-time relation of a MMC specimen are shown in Fig. 3 where two cases are shown: with air cooling (dashed line) and without air cooling (solid line). In the present study, T_{max} is set equal to 1100°C, while three different T_{min} are used: 352, 534, and 800°C.

The longitudinal (axial) length of the MMC specimen is measured before and after thermal cycles with a needlepoint micrometer. The resolution of the micrometer is approximately 20 μm. With a specimen gauge length of 28 mm, the smallest resolvable difference in the data is approximately 0.001. A summary of longitudinal (axial) dimensional change ($\Delta''/''$) where Δ'' and $''$ are the change in length, and initial length of a specimen, respectively is given in Table 3. The test specimen ID number in Table 3 is defined such that the first letters stands for type of MMC, the first number for T_{max}, and the second number for T_{min}. Some of MMC specimens tested under severe conditions exhibited excess damage, thus those specimens are not usable for measurement of dimensional changes (marked by * in Table 3).

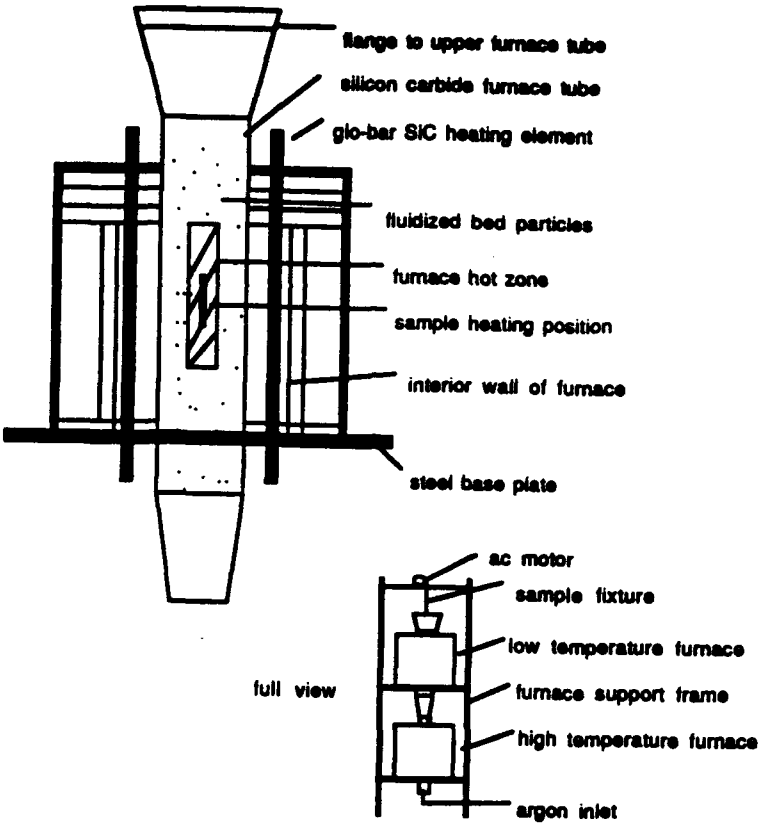

Figure 2. Schematic Diagram of the Metallurgical Thermal Cycling Machine.

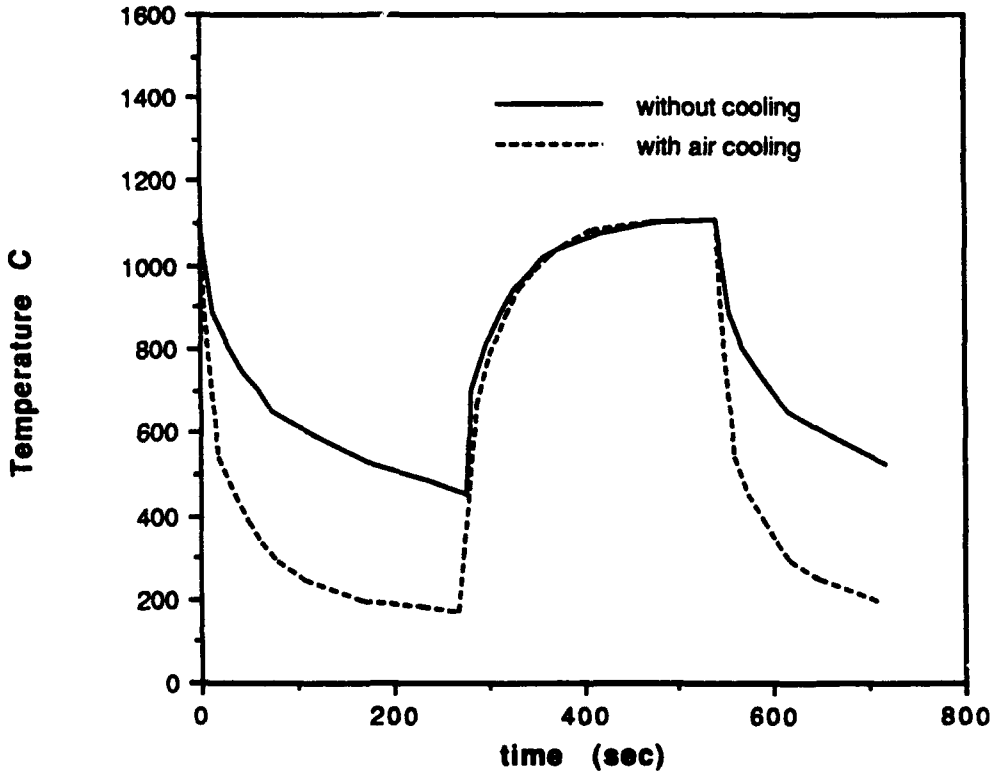

Figure 3. Creep Thermal Cycling Machine Time Temperature History.

Table 3. Longitudinal Dimensional Change (Strain)

	Test Specimen ID Number	100 Cycles	500 Cycles	750 Cycles
Continuous fiber MMC	CF-1100-352	.004683	.02442	*
	CF-1100-534	.002257	.00755	*
	CF-1100-800	—	damaged	*
Aligned short fiber MMC	ASF-20-1100-352	.004252	.01494	*
	ASF-20-1100-352	—	.01577	
	ASF-20-1100-534	.01080	.02512	*
	ASF-20-1100-800	—	.007162	*
	ASF-5-1100-352	−.000644	.000270	.00670
	ASF-5-1100-534	.000911	.002523	.01514
	ASF-5-1100-800	—	.003892	—
Hybrid composite	AF-1100-352	−.001606	−0.000966	.00734
	AF-1100-534	−.000588	.002151	.01203
	AF-1100-800	—	.000535	—

Those specimens marked by – sign were not tested due to limited number of specimens. The results of the axial dimensional change of the four types of MMC specimens with T_{min} = 352°C and T_{max} = 1100°C are plotted as a function of the number of thermal cycles (N) in Fig. 4. Figure 4 indicates that the increasing order of axial dimensional changes observed is continuous fiber MMCs (CF), aligned short fiber MMCs with fiber aspect ratio 20 (ASF-20), and with 5 (ASF-5), and hybrid composite which is a combination of ASF-20 and 10% volume chopped Al_2O_3 fibers in the matrix (AF). This order is expected since the CTE mismatch strain is larger for CF than for both ASF-5 and AF. Table 2 also shows their volume fractions, CF having 31.9% (largest) and the other having almost the same volume fraction (≈ 19%). A comparison between the experimental and analytical results of dimensional change will be given in Section 4.

2.4 Observation of Damages

In order to assess the extent of the damages induced in the thermally cycled MMCs, we observed both uncycled and cycled MMC specimens by optical microscope, scanning electron microscope (SEM) and transmission electron microscope (TEM).

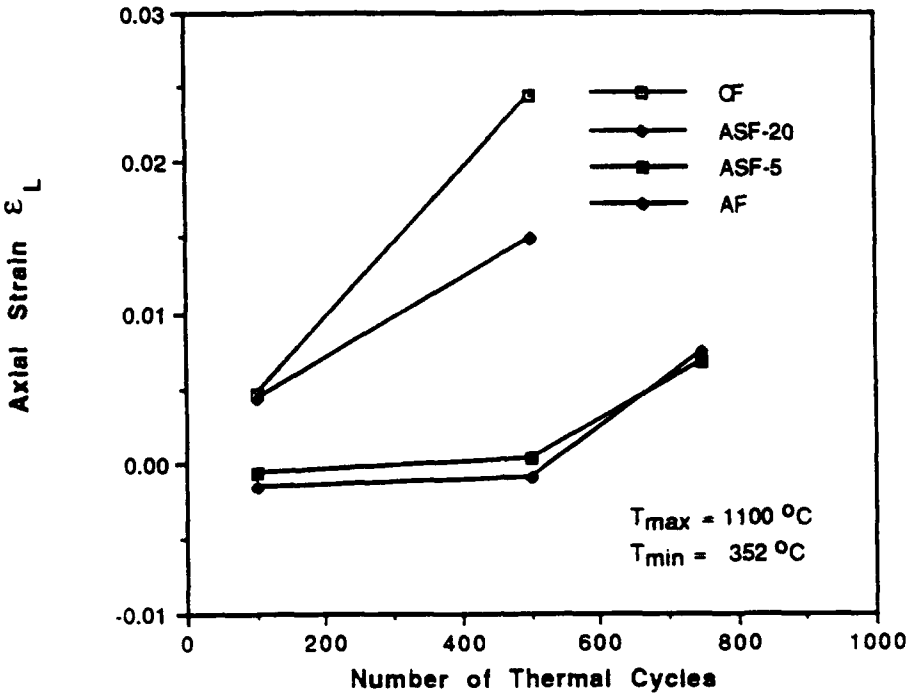

Figure 4. Axial Strain Change Versus Number of Thermal Cycles, 1100-352 °C.

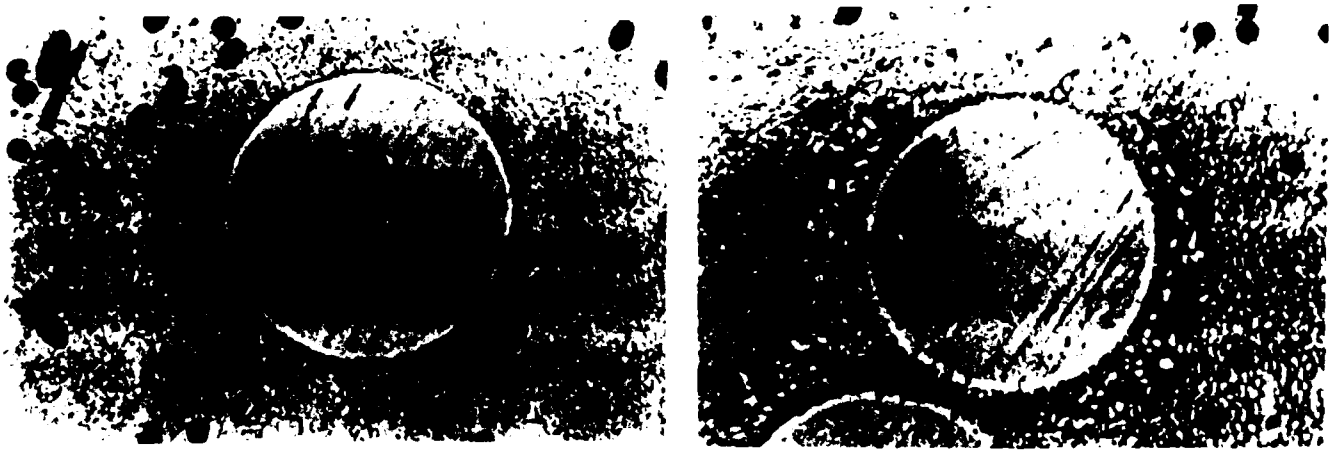

(a) (b)

Figure 5. Scanning Electron Micrographs of Hybrid Composite Microstructure, (a) As HIPed, (b) After 500, 1100-352 °C Thermal Cycles.

Figure 5 shows a normal view of a hybrid MMC (AF) specimen obtained by an optical microscope where (a) and (b), denote the as-received and 500 cycled specimens, respectively. It is noted in Fig. 5 that the dark islands of elliptical shape are the chopped Al_2O_3 fibers mixed with the matrix. All the thermal cycled MMC specimens were subjected to the same thermal cycling conditions: T_{max} = 1100°C, T_{min} = 352°C, and with high temperature duration of τ = 4 minutes. From the micrographs taken from the as-processed and thermal cycled MMCs, one can characterize the micro-damage associated with the as-received and as-thermally cycled MMCs. The thickness of circumferential reaction zone and crack density (number of cracks per fiber) within the zone are measured as a function of number of thermal cycles, and the results are plotted in Fig. 6(a) and (b), respectively. Figure 6 indicates that hybrid composite (AF) exhibited the best performance among the others whereas CF and ASF-20 give rise to larger crack density and thicker reaction zone.

A limited amount of TEM study was conducted on the thermal cycled ASF-20 and AF specimens[19] with the aim of determining the effect of Al_2O_3 fibers added to AF specimen in terms of dislocation morphology. Figures 7(a) and (b) show TEM photographs of the dislocation morphology of the matrix-reaction zone interface in the ASF-20 specimen and that of the matrix-Al_2O_3 fiber interface in the AF specimens, respectively. These TEM photos suggest that the addition of Al_2O_3 chopped fibers into the matrix of the AF (hybrid) specimen relaxes the otherwise high stress concentration at the matrix-W-ThO_2 fiber interface induced by the punching of dislocations [20] by the CTE mismatch strain. At the same time, the matrix with Al_2O_3 fibers becomes strengthened. These mechanisms contribute to the increase in thermal cycling resistance of hybrid MMC.

In order to obtain some clues to the accelerated rate of dimensional changes observed in the thermally cycled MMCs with higher number of cycles, Fig. 8, we conducted SEM observations on longitudinal sections of the cycled specimens, focusing on the matrix-fiber (W-ThO_2) interface. To this end, numerous SEM photographs were taken along the interfacial zones of ASF-5, ASF-20, and AF specimens. Figures 9(a) and (b) show the SEM micrographs of the interface near the fiber-end of the as-processed and thermal-cycled N=500) ASF-5 specimen, respectively. It is clearly observed in Fig. 9 that thermal cycling to N = 500 resulted in debonding of the matrix-fiber interface. In order to

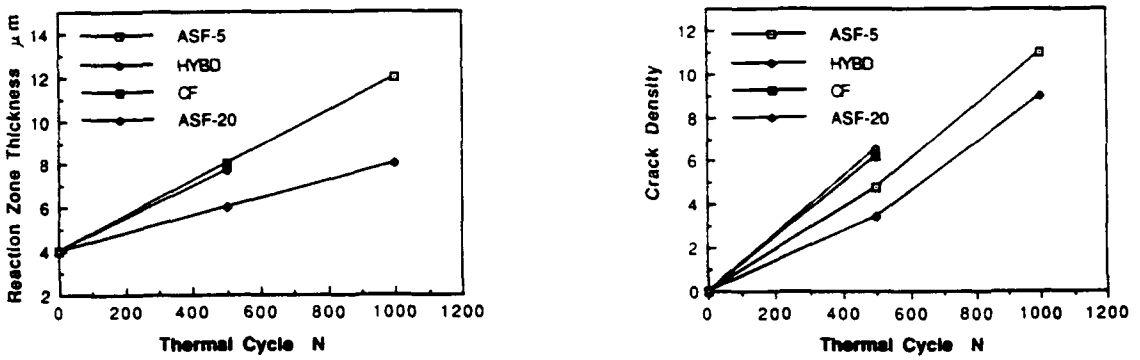

(a) (b)

Figure 6. Microstructural Changes as a Function of Number of Thermal Cycles. (a) Thickness of Reaction Zone, (b) Crack Density.

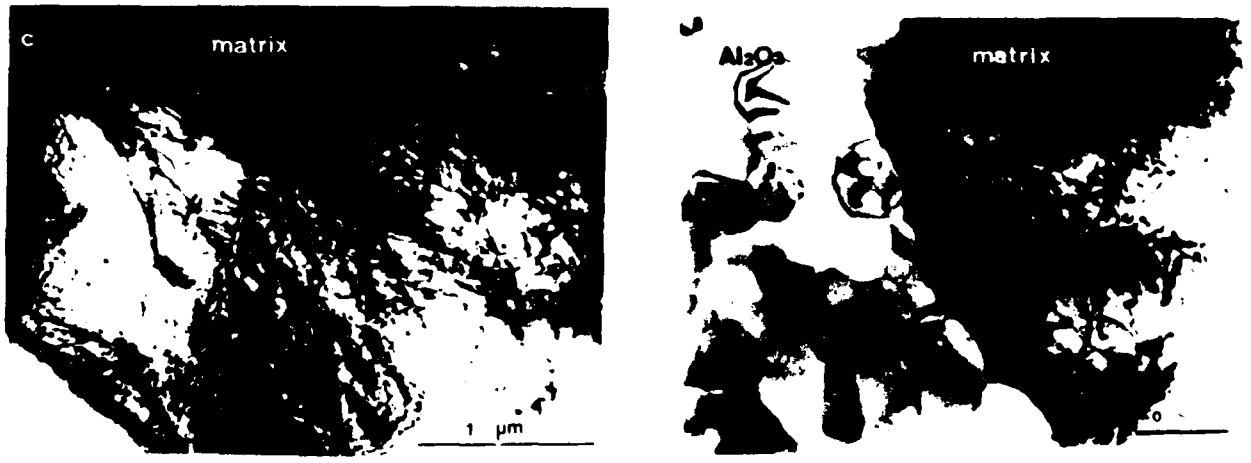

(a) (b)

Figure 7. Transmission Electron Micrographs of Thermal Cycled Composite, (a) W(Fe,CR) Reaction Zone -FeCrAlY Matrix Interface, (b) Al_2O_3-FeCrAlY Interface.

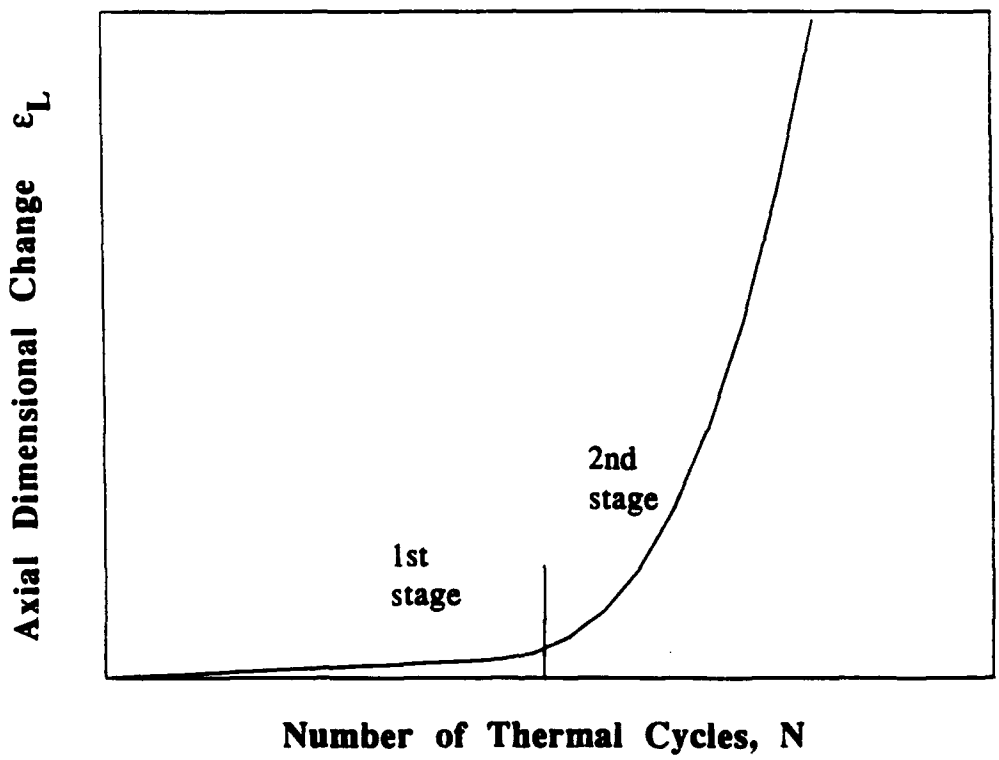

Figure 8. Dimensional Change as a Function of Thermal Cycles, Non-Linear for the Second Stage.

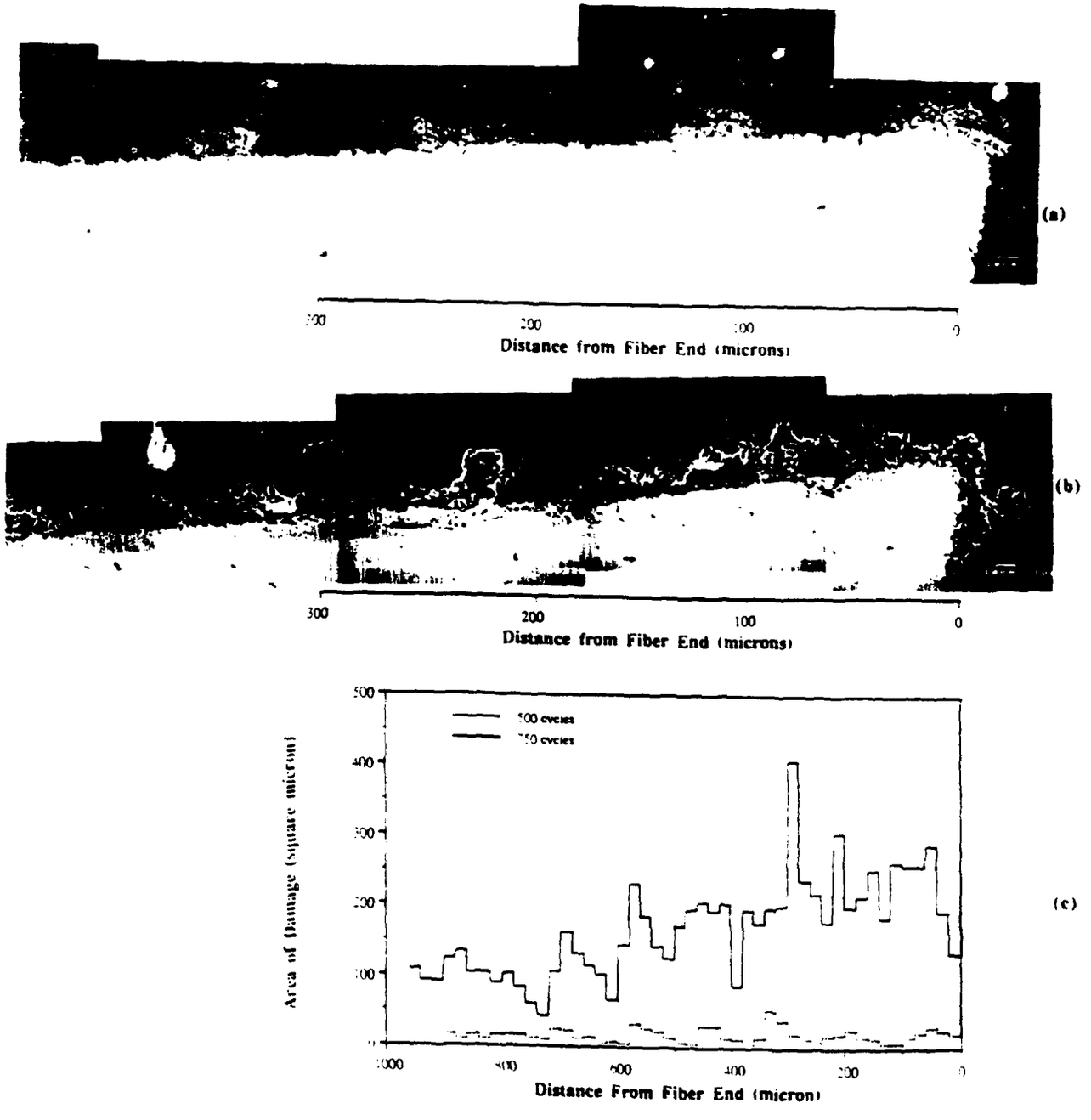

Figure 9. SEM Photographs Showing Thermal Cycling Induced Interfacial Damage and Results of Damage Quantification by Image Analysis.

quantify the damage near the interface, the SEM photographs enhanced to provide black and white pictures where black domains denote voided (or damaged) area. The enhanced pictures were scanned by an Apple scanner connected to Macintosh-II computer system to create a scan file where each black pixel represented 0.0675 square micron of damage. By using computer software developed to count the number of black pixels in the scanfile, we converted the damage profile shown in the SEM photographs to an area distribution of damage along the fiber length. Examples of the area distribution of damage are shown in Fig. 9(c) where the dashed and solid lines denote the damage area of the 500 and 750 cycled ASF-5 specimens, respectively. Figure 10 shows a comparison of the damage area plots of ASF-20 and hybrid MMCs, both thermal cycled to N = 500. Figures 9 and 10 indicate that for N = 500, the hybrid composite gives rise to the smallest amount interfacial damage while the ASF-20 specimen yields the largest amount of damage. Thus for the same fiber aspect ratio (= 20), the thermal cycling resistance of the hybrid composite improved over that of the non-hybrid composite (ASF-20). It follows from Figs. 9 and 10 that the extent of the damaged area is the largest for the ASF-20 specimens and is the smallest for the AF specimen. The thermal cycling damage appears to start from fiber-ends and progressively extends towards the center of fiber as the number of thermal cycles increases. This is illustrated schematically in Fig. 11. This interfacial damage reduces the load transfer capacity from the matrix to the short fiber which is a key strengthening mechanism for short fiber MMCs. The damage would also have a strong effect on the dimensional change.

3. ANALYTICAL MODEL

The present analytical model is aimed at predicting dimensional changes induced in thermally cycled MMCs. Typical experimental data of axial dimensional change (ε_L) of several MMCs is summarized by Fig. 8: The ε_L – N curve consists of basically two stages, the first stage is where the ε_L – N relation is linear, the second stage where it becomes highly non-linear indicating progressive damage. The first stage corresponds to the case of perfectly bonded interfaces, while the second stage to the case of progressively debonded interfaces. We shall treat these two cases separately in the following. Most

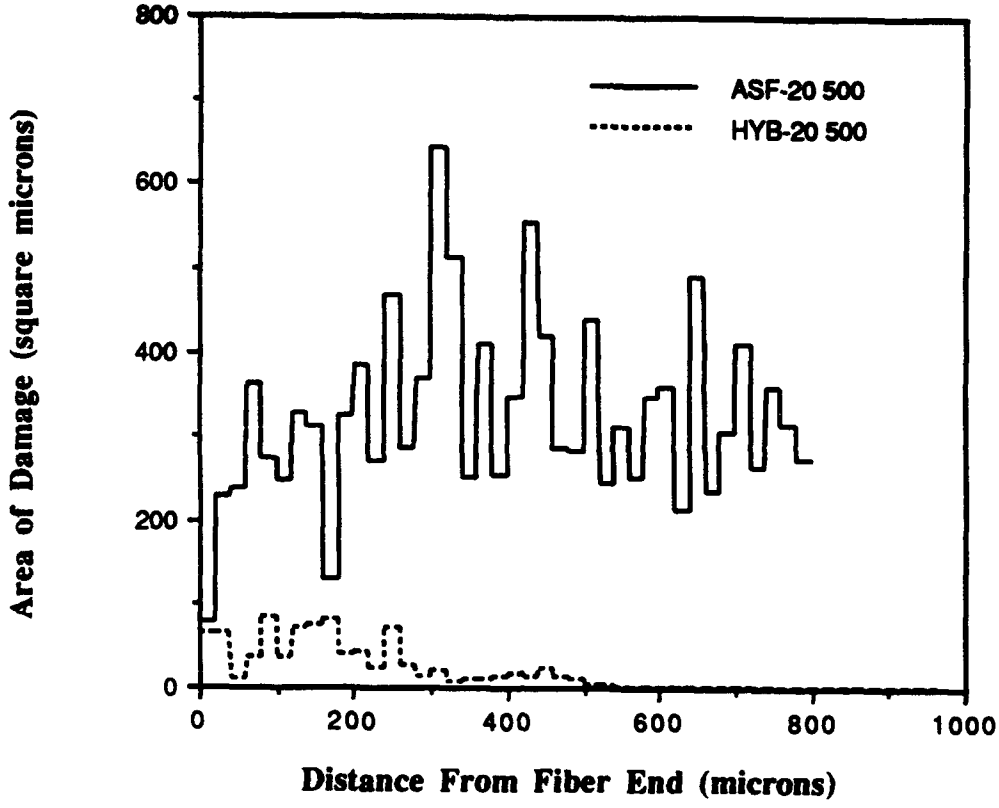

Figure 10. Interfacial Damage Quantification by Image Analysis Comparing Thermal Cycled Non-Hybrid and Hybrid, Aspect Ratio 20 Composite Materials.

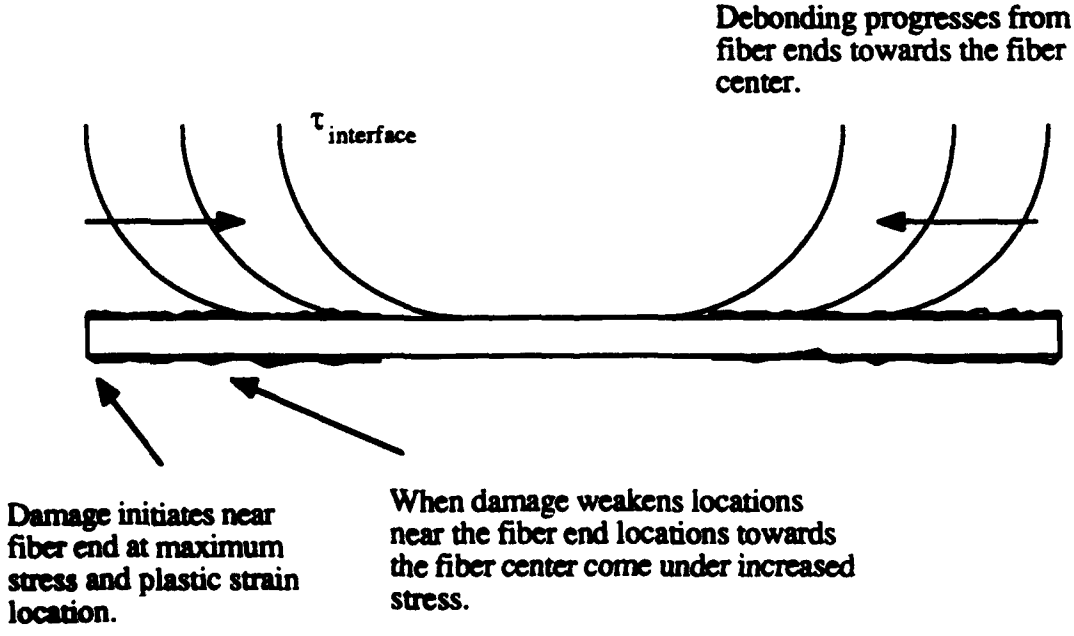

Figure 11. Progressive Interfacial Damage Mode During the Second Stage of Thermal Cycling Deformation.

of the formulation used in the analytical model for the first stage, however, can also be used for the second-stage model.

3.1 Analytical Model for Perfectly Bonded Interface

The temperature-time history for thermal cycling is idealized as shown in Fig. 12 where the specimen is initially subjected to T_{max} at which it is assumed stress-free, and then experiences the temperature sequence: $a \rightarrow b \rightarrow c \rightarrow d \rightarrow e$.

The main assumptions used in the present model are:

(1) For the cooling process ($a \rightarrow b$), $T_{max} - T_{min}$ is large enough to yield the matrix metal of the MMC with yield stress (σ_y) at some temperature (T_{yield}) while the fiber remains elastic throughout the cycle.

(2) At T_{max}, the matrix can yield with the high temperature yield stress (σ_y^{HT}) and also can creep according to a power-law of the Dorn type.[22]

(3) For the majority of the analysis, short fibers are aligned in one direction, Fig. 13. We will discuss later the effect of fiber misorientation on dimensional change, Fig. 14.

(4) Both the matrix and fiber are isotropic in stiffness (E , v) and CTE(α).

<u>*Cooling Process a → b*</u>

Referred to Fig. 12, as the temperature drops from T_{max} to T_{min}, the matrix metal undergoes two different deformations: elastic (from $T_{max} \rightarrow T_{yield}$) and plastic ($T_{yield} \rightarrow T_{min}$). Hence, we will first determine T_{yield} at which the matrix starts yielding. The CTE mismatch strain that exists in the domain of fiber, $\underset{\sim}{\alpha}^*$ can be given by

$$\underset{\sim}{\alpha}^* = (\alpha_f - \alpha_m, \alpha_f - \alpha_m, a_f - \alpha_m , 0, 0, 0)\, \Delta T \qquad (1)$$

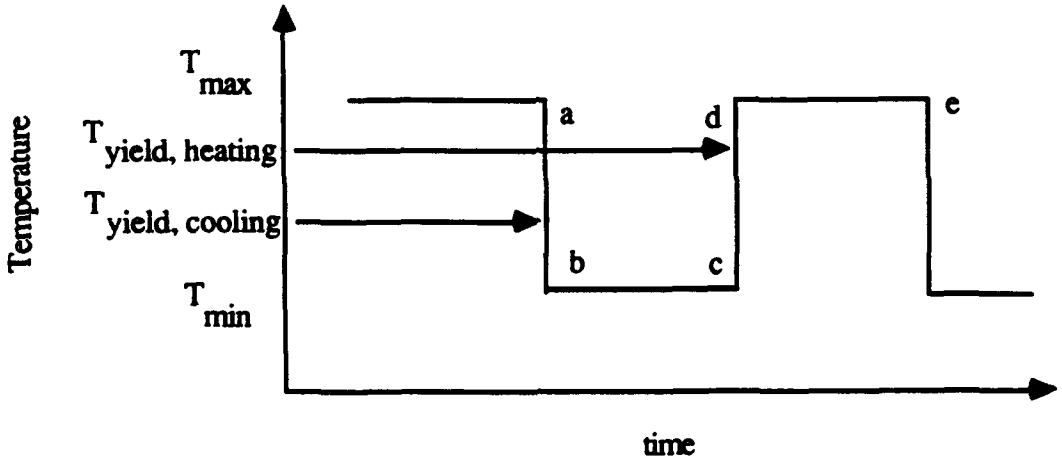

Figure 12. Idealized Time (t) versus Temperature (T) Relation Used in the Present Model.

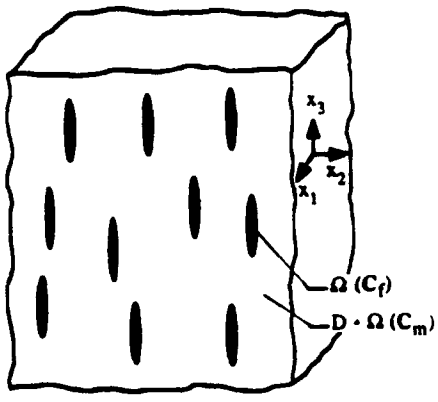

Figure 13. Domain of the Analytical Model for an Aligned Short Fiber MMC and Definitions of Coordinate System Used.

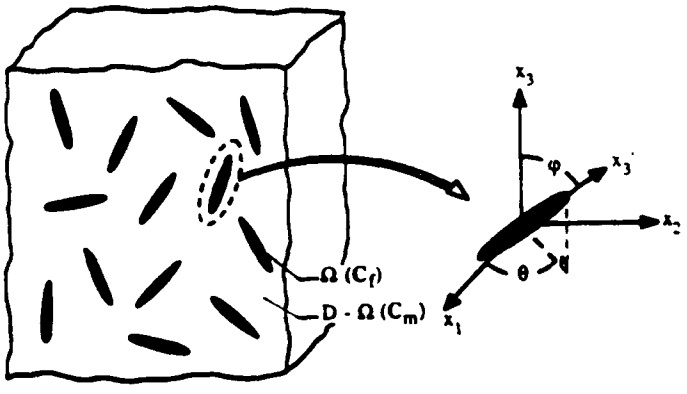

Figure 14. Domain of the Analytical Model for a Misoriented Short Fiber Composite and Definition of Coordinate System Used.

where the components of $\underset{\sim}{\alpha}^*$ are 11, 22, 33, 23, 31, and 12, from the right to left in order. In eq. (1) α_f and α_m are the CTEs of the fiber and matrix, respectively, and ΔT is the temperature change (equal to $T_{yield} - T_{max}$, in the case of the cooling process a → y). The volume averaged stress in the fiber $\underset{\sim}{\sigma}_f^y$ and matrix, $\underset{\sim}{\sigma}_m^y$ are calculated using the Eshelby's equivalent inclusion method, (30) see Appendix A, where the eigenstrain $\underset{\sim}{e}_T$ is replaced by $\underset{\sim}{\alpha}^*$, Eq. (1).

$$\underset{\sim}{\sigma}_f^y = (1-f)\, \underset{\sim}{C}_m \cdot (\underset{\sim}{S} \cdot \underset{\sim}{e}^* - \underset{\sim}{e}^*) \tag{2}$$

$$\underset{\sim}{\sigma}_m^y = -f\, \underset{\sim}{C}_m\, (\underset{\sim}{S} \cdot \underset{\sim}{e}^* - \underset{\sim}{e}^*) \tag{3}$$

where $\underset{\sim}{C}_m$ is the stiffness tensor of the matrix (Young's modulus E_m and Poisson's ratio ν_m for isotropic matrix), $\underset{\sim}{S}$ is Eshelby's tensor which is a function of the fiber aspect ratio ("/d) and ν_m whose explicit expression has been given elsewhere[1]. In eqs. (1) and (2) $\underset{\sim}{e}^*$ is the fictitious eigenstrain introduced into the fiber domain (see Appendix A). The dots used in Eqs. (2) and (3) are inner product between tensors, and used throughout this paper. For the matrix to yield at T_{yield}, $\underset{\sim}{\sigma}_m^y$ must satisfy the yield condition:

$$\frac{3}{2}\, \underset{\sim}{\sigma}_m^{y'} \cdot \underset{\sim}{\sigma}_m^{y'} = \underset{\sim}{\sigma}_y^2 \tag{4}$$

where σ_y is the matrix yield stress at T_{yield} (set equal to T_{min} for simplicity in the analysis), and $\sigma_m{}^{y\cdot}$ is the deviatoric component of $\sigma_m{}^{y\cdot}$. Eq. (4) provides the value of T_{yield}. As the temperature is further reduced from T_{yield} to T_{min}, the corresponding CTE mismatch strain $\underset{\sim}{\alpha}^*$ will be used to generate plastic strain, $\underset{\sim}{\varepsilon}^P$ at T_{min} with its components given by

$$\underset{\sim}{\varepsilon}^P = (-e_p/2,\ -e_p/2,\ e_p\ 0,\ 0,\ 0) \tag{5}$$

where e_p denotes the axial component of the plastic strain (i.e., along the x_3-axis, Fig. 13), which is still unknown at this stage of the formulation, but will be determined as follows. A given plastic strain in the matrix induces the internal stress in the matrix ($\underset{\sim}{\sigma}_m^p$) and in the fiber ($\underset{\sim}{\sigma}_f^p$) which can be calculated by the Eshelby's equivalent inclusion

method, as shown in Appendix A where $\underset{\sim}{\varepsilon}_T = -\underset{\sim}{\varepsilon}_p$. The average stress in the matrix at T_{min} is the sum of $\underset{\sim}{\sigma}_m^P$ and $\underset{\sim}{\sigma}_m^T$, the latter being the thermo-elastic stress obtained for $\underset{\sim}{\varepsilon}_T = \underset{\sim}{\alpha}^*$ with $\Delta T = T_{min} - T_{max}$. Assuming a perfectly plastic matrix, this average matrix stress at T_{min} (its axial and transverse components being σ_{m33} and σ_{11}, respectively) must satisfy the yield condition:

$$\sigma_{m33} - \sigma_{m11} = \sigma_y \tag{6}$$

Eq. (6) then provides the value of e_p, which will contribute to the macroscopic plastic strain of the MMC at T_{min} (stage b).

$$\varepsilon_L^P = (1-f)e_p$$

$$\varepsilon_T^P = -(1-f)e_p/2 \tag{7}$$

where the subscripts L and T denote the component along the longitudinal (axial, or x_3) and transverse, or x_1–, x_2–) axes, respectively.

Heating process c → d

As the temperature changes rapidly from T_{min} (stage c) to T_{max} (stage d), the CTE mismatch strain defined by Eq. (1) with $\Delta T = T_{max} - T_{min}$ induces the internal stress in the fiber and matrix. Hence the average stress in the matrix at stage d becomes $\underset{\sim}{\sigma}_m^P$, since $\underset{\sim}{\sigma}_m^T$ cancels with that induced during the cooling process (c → d). The matrix average stress $\underset{\sim}{\sigma}_m^P$ must satisfy the yield condition at T_{max} if its effective stress exceeds the high temperature yield stress σ_y^{HT}. This can be accomplished by introducing an additional plastic strain in the matrix, $\underset{\sim}{\varepsilon}^{HIP}$.

The average matrix stress induced by $\underset{\sim}{\varepsilon}^{HTP}$ (denoted by $\underset{\sim}{\sigma}_m^{HTP}$) can be calculated by Eq. (A1) where ε_T is replaced by $\underset{\sim}{\varepsilon}^{HTP}$. Then, the total averaged stress in the matrix at stage d, is $\underset{\sim}{\sigma}_m^P + \underset{\sim}{\sigma}_m^{HTP}$ which must satisfy the yield condition:

$$(\sigma^{P}_{m33} + \sigma^{HTP}_{m33}) - (\sigma^{P}_{m11} + \sigma^{HTP}_{m11}) = -\sigma^{HT}_{y} \tag{8}$$

It should be noted here that the effective (flow) matrix stress at stage d is compressive.

Additional plastic strain at stage d, $\underset{\sim}{\varepsilon}^{HTP}$ contributes to the macroscopic plastic strain, $\underset{\sim}{\varepsilon}^{HTP}$ (longitudinal composite denoted by ε^{HTP}_{L} and transverse component by ε^{HTP}_{T}),

$$\varepsilon^{HTP}_{L} = (1-f)e_{HTP}$$

$$\varepsilon^{HTP}_{T} = -(1-f)e_{HTP}/2 \tag{9}$$

At the end of stage d, the matrix flow stress is equal to σ^{HT}_{y}.

High temperature plateau: d → e

During the isothermal exposure at T_{max}, the matrix metal stress creeps to reduce its flow stress. In order to simulate the creep relaxation process of the matrix, we shall subdivide the duration of the high temperature plateau (τ) into m time increments. For each time increment Δt, the following Dorn type creep law of Dorn type[22] is applied to calculate the resulting creep strain increment.

$$\Delta e_c = -\left\{A\left(\frac{\sigma_m}{G}\right)^n \frac{G\,b\,D_o}{k\,T_{max}} \exp\left(\frac{Q_v}{R\,T_{max}}\right)\right\}\Delta t \tag{10}$$

where

Δe_c = incremental axial creep strain
A = Dorn constant
σ_m = matrix flow stress
G = matrix shear modulus
b = matrix Burgers vector

k = Boltzman's constant

D_o = pre-exponential constant for self-diffusion

R = gas constant

n = power law constant

Q_v = activation energy

The minus sign on the right hand side of Eq. (10) indicates that the matrix is in compression during the high temperature plateau. Once the creep strain increment Δe_c is obtained from Eq. (10), we will calculate the stress induced by Δe_c, $\Delta \underset{\sim}{\sigma}_m$ by Eq. (A2) where

$$\underset{\sim}{e}_T = \Delta \underset{\sim}{e}^c$$

and where

$$\Delta \underset{\sim}{e}^c = (-\Delta e_c/2,\ -\Delta e_c/2,\ \Delta e_c,\ 0,\ 0,\ 0) \tag{11}$$

Then, the total averaged stress in the matrix becomes $\underset{\sim}{\sigma}_m + \Delta \underset{\sim}{\sigma}_m$, from which the matrix flow stress in the next incremental step, σ_m' is calculated as

$$\sigma_m' = (\sigma_{m33} + \Delta\sigma_{m33}) - (\sigma_{m11} + \Delta\sigma_{m11}) \tag{12}$$

σ_m' will then be substituted into Eq. (10) to calculate the next incremental creep strain. At the end of the incremental process, i.e., at stage e, the total creep strain along the x_3–axis becomes

$$e_c = \sum_{i=1}^{m} \Delta e_c \tag{13}$$

$\underset{\sim}{e}_c$ contributes to the macroscopic plastic strain of the MMC, $\underset{\sim}{\varepsilon}^c$ with its longitudinal ε_L^c and transverse component ε_T^c given by

$$\varepsilon_L^c = (1-f)e_c$$

$$\varepsilon_T^c = -(1-f)e_c/2 \qquad (14)$$

Dimensional Change per Cycle, $\Delta\varepsilon$

At the completion of one thermal cycle, i.e., at stage e, the total plastic strain $\Delta\underset{\sim}{\varepsilon}$ (dimensional change per cycle) can be calculated from Eqs. (7), (9), and (14).

Along the fiber axis:

$$\Delta\varepsilon_L = \varepsilon_L^p + \varepsilon_L^{HTP} + \varepsilon_L^c \qquad (15a)$$

Along the transverse direction:

$$\Delta\varepsilon_T = \varepsilon_T^p + \varepsilon_T^{HTP} + \varepsilon_T^c \qquad (15b)$$

Eq. (15) provides the dimensional change of an MMC for the first stage of ε_L – N curve where the matrix-fiber interface is presumably well bonded.

3.2 Analytical Model for Progressively Debonded Interface

The formulation derived for the case of perfectly bonded interfaces can be applicable to that of progressive debonded interface with minor modification. The modification is to account for the effective volume fraction of fiber f_e for the composite with debonded interfaces. f_e depends on the extent of the debonded interfaces. Since the stress concentration is highest at fiber-ends, the debonding is more likely to take place there first, and then extends toward the fiber center as evidenced by SEM photographs, Fig. 9.

During the cooling process (a → b, Fig. 12), the radial stress (σ_{rr}) induced at the matrix-fiber interface due to CTE mismatch is compressive, while for the heating period

($c \rightarrow d$), σ_{rr} at the interface becomes compressive.[23] This leads to the length of the debonded interface (d") for cooling being smaller than that for heating. The matrix material adjacent to the tip of the debonding is subjected to the highest shear stress (or strain, $\Delta\gamma$) which repeats between opposite signs. Therefore, the location of the tip at stage a (the beginning of each cycle) will extend progressively with accumulated number of cycles N due to the propagation law of low cycle fatigue given by[17]

$$\Delta\gamma = \gamma_F(2N)^{\alpha} \tag{16}$$

where γ_F is the fracture shear strain in a static shear test ($2N = 1$) and α is material constant. The sequence of progressive debonding interfaces is schematically shown in Fig. 15 where the cycles (N-1) $\rightarrow$ N $\rightarrow$ (N+1) are considered. The lengths of the debonded interface during the cooling ($a \rightarrow b$) and heating ($c \rightarrow d \rightarrow e$) at N cycles are denoted by $d"^{-}_{N}$ and $d"^{+}_{N}$, respectively.

The superscripts (+) and (–) corresponds to the radial stress at the interface being in tension and compression, respectively. It is noted in Fig. 15 that $d"^{+}_{N+1} > d"^{+}_{N} > d"^{+}_{N-1}$, indicating that the debonding progresses with N. In reality, this is governed by Eq. (16), thus the extension may take place only after a critical number of accumulated cycles. Due to the unavailability of the low cycle data (Eq. (16)), we employ here the assumption that the extension is a continuous process with N. The change in the length of the debonded interface $d"_N$ is directly related to that of the effective fiber length $"_N$, which in turn can be interpreted as that in the effective volume fraction of fiber, f_N.

It is clear from Eqs. (7), (9), (14), and (15) that the accumulated inelastic strain per cycle, $\Delta\varepsilon$ is dependent on (1–f) where f is the effective volume fraction of fiber, thus equal to f_N for a given cycle N. It should be noted again that f_N is not constant during this cycle N: it is larger for the cooling period than for the heating period and high temperature

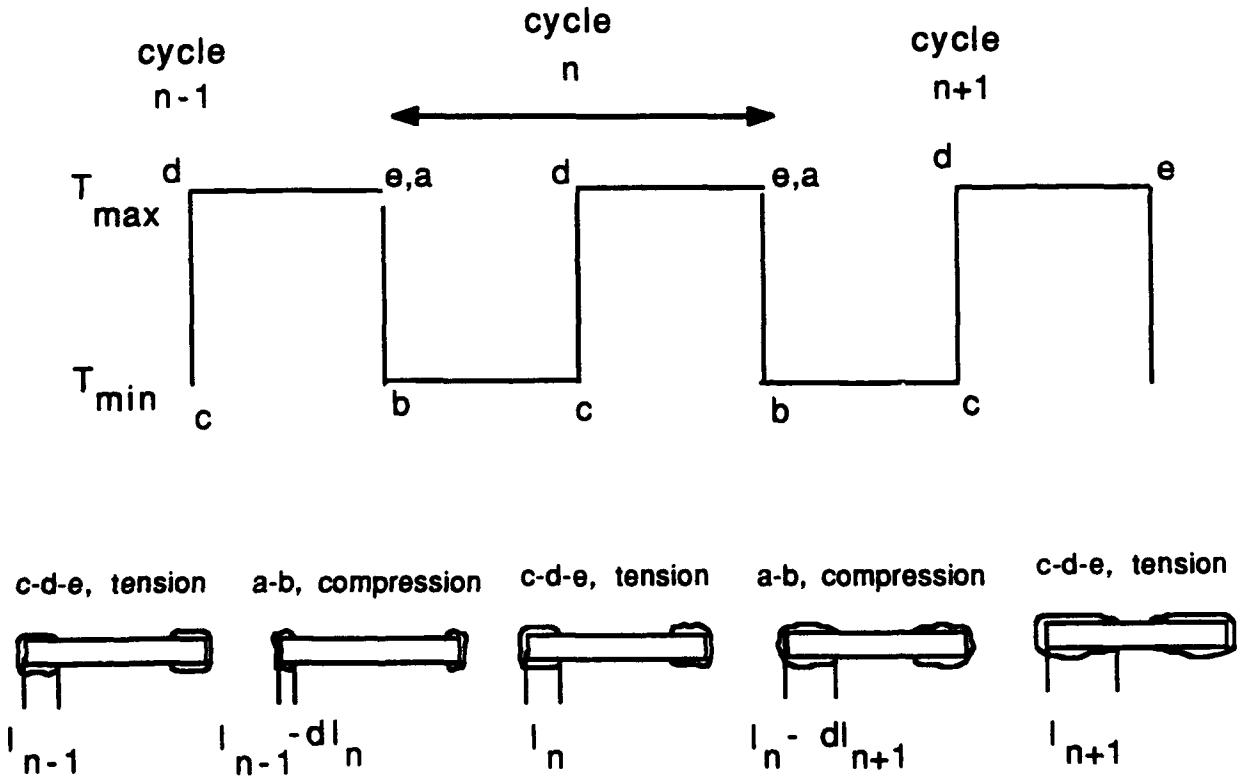

Figure 15. Progressive Debonding of Fiber Interfaces in a Thermal Cycled Composite.

plateau, Fig. 15. With this in mind, one can express the longitudinal dimensional change per cycle during the Nth cycle as:

$$\Delta\varepsilon_L^N = (1-f_N^+)\, e_p + (1-f_N^-)\,(e_{HTP} + e_c) \tag{17}$$

where f_N^+ and f_N^- are the effective volume fractions during the Nth cycle during the cooling ($a \rightarrow b$) and heating and high temperature plateau ($c \rightarrow d \rightarrow e$), respectively.

In actual computation, one must specify the rate of change of effective fiber volume fraction between N and N+1 cycles focusing on the compression (a–b) period, df_N is defined as

$$df_N = f_{N+1}^- - f_N^- \tag{18}$$

One also needs to specify the differences in f_N between the heating (c–d→ e) and cooling (a→b) periods, Δf_N given by

$$\Delta f_N = f_N^+ - f_N^- \tag{19}$$

With the values of df_N and Δf_N given, one can calculate the dimensional change for the N-th cycle, $\Delta\varepsilon^N$. Then the accumulated dimensional change up to N cycles, ε^N is given by

$$\varepsilon^N = \sum_{i=1}^{N} \Delta\varepsilon^i \tag{20}$$

4. DISCUSSION

To ensure the validity of the present model, we shall compare predictions by the present model with those of existing models, with the experimental results reported by others, and with the present experimental results. We will discuss the predictions for

the first stage of ε–N curve in Subsection 4.1, followed by those for the second stage in Subsection 4.2.

4.1 Dimensional Change for the First Stage

The other models with which we shall compare results from the present one are Garmong's model,[24] the Yoda et al. model,[6] and Taya-Mori model.[25] For the purpose of comparison, we use the data of a hypothetical MMC (continuous fiber) given by Garmong:

CTE mismatch:	$\alpha_m - \alpha_f = 10 \times 10^{-6}/K$
fiber volume fraction:	$f = 0.5$
matrix Young's modulus:	$E_m = 6.9 \times 10^4 MPa$
matrix shear modulus:	$G_m = 2.62 \times 10^4 MPa$
fiber Young's modulus:	$E_f = 2.1 \times 10^5 MPa$
matrix yield stress:	$\sigma_y = 0.56 - 0.07 \times T$ (MPa)
constants of matrix flow stress–plastic strain relations*:	$K^* = 690MPa$ $n = 0.5$
creep constants**	$D_o A G_b / k = 3.1 \times 10^{26}/sec$ $Q/R = 17600K$ $s = 4.4$
Thermal cycling condition:	$T_{max} = 700K$ $T_{min} = 300K$ $\tau = 60$ sec

where * and ** denote

$$\sigma_m = \sigma_y + K^* e_p^n$$

and the creep law of Dorn type defined by Eq. (10), respectively.

With regard to Garmong's model, we shall use the model corrected by Tyson.[27] Analytical results of dimensional change by the Yoda et al. model cannot be obtained by

straight application of the Garmong data, thus, we use here the upperbound of the dimensional change by the Yoda et al. model.[6]

$$\Delta\varepsilon_L^{UB} = \frac{\sigma_y^{HT}}{E_m}\left\{1 + \frac{1-f}{f}\cdot\frac{E_m}{E_f}\right\} \tag{21}$$

where σ_y^{HT} is the matrix yield stress at T_{max}. The results of dimensional change per cycle, $\Delta\varepsilon_L$, of the hypothetical MMC are plotted as a function of fiber volume fraction, f, in Fig. 16 where (a) and (b) cover the entire range of f, and the range of f focused on the $\Delta\varepsilon_L$ peak values (f = 0 ~ 0.1), respectively. In the figure, the results of the Garmong model multiplied by (1–f) are also shown, which becomes zero as f approaches 1. It is noted in Fig. 16 that the results of $\Delta\varepsilon_L^{UB}$ by Yoda et al. model lie far above those of the other models and do not possess a peak like the others. Moreover it does not converge to zero as $f \rightarrow 1$. It also follows from Fig. 16 that the dimensional change per cycle by both Garmong and Taya-Mori models do not approach to zero as $f \rightarrow 1$. The present model exhibits the correct tendency: $\Delta\varepsilon_L \rightarrow 0$ as $f \rightarrow 1$, indicating that the present model can account for the interaction between fibers at higher volume fractions. An important implication of Fig. 16 is that there exists a peak value of $\Delta\varepsilon_L$ corresponding to a small volume fraction of fiber, $f \cong 0.06 \sim 0.065$. It would be wise then for us to avoid this critical volume fraction to minimize the dimensional change. The effect of fiber aspect ratio predicted by the present model for the Garmong's data with f = 0.2 is examined and the results are shown in Fig. 17, suggesting several important conclusions: (1) for aspect ratios ("/d) larger than 6, $\Delta\varepsilon_L$ is not sensitive to "/d, (2) $\Delta\varepsilon_L$ has a peak at about "/d = 1.6, and (3) a particle MMC where the reinforcement aspect ratio is 1, would not give rise to any dimensional change. The last conclusion, however, does not lead to the conclusion that particle MMC is free of thermal cycling damage; instead, the cyclic stress in an around a particle due to thermal cycling may result in the debonding of the matrix-particle interface.

A limited amount of experimental data are available in the literature on dimensional change of thermally cycled MMCs during the first stage (Figure 8). These studies include the investigation of W/Cu by Yoda et al.[6], SiC_w/Al by Patterson and Taya,[12] and the present experimental study on W-1%ThO_2/FeC_rAlY. The input data of these MMC systems for the present model are summarized in Table 4.

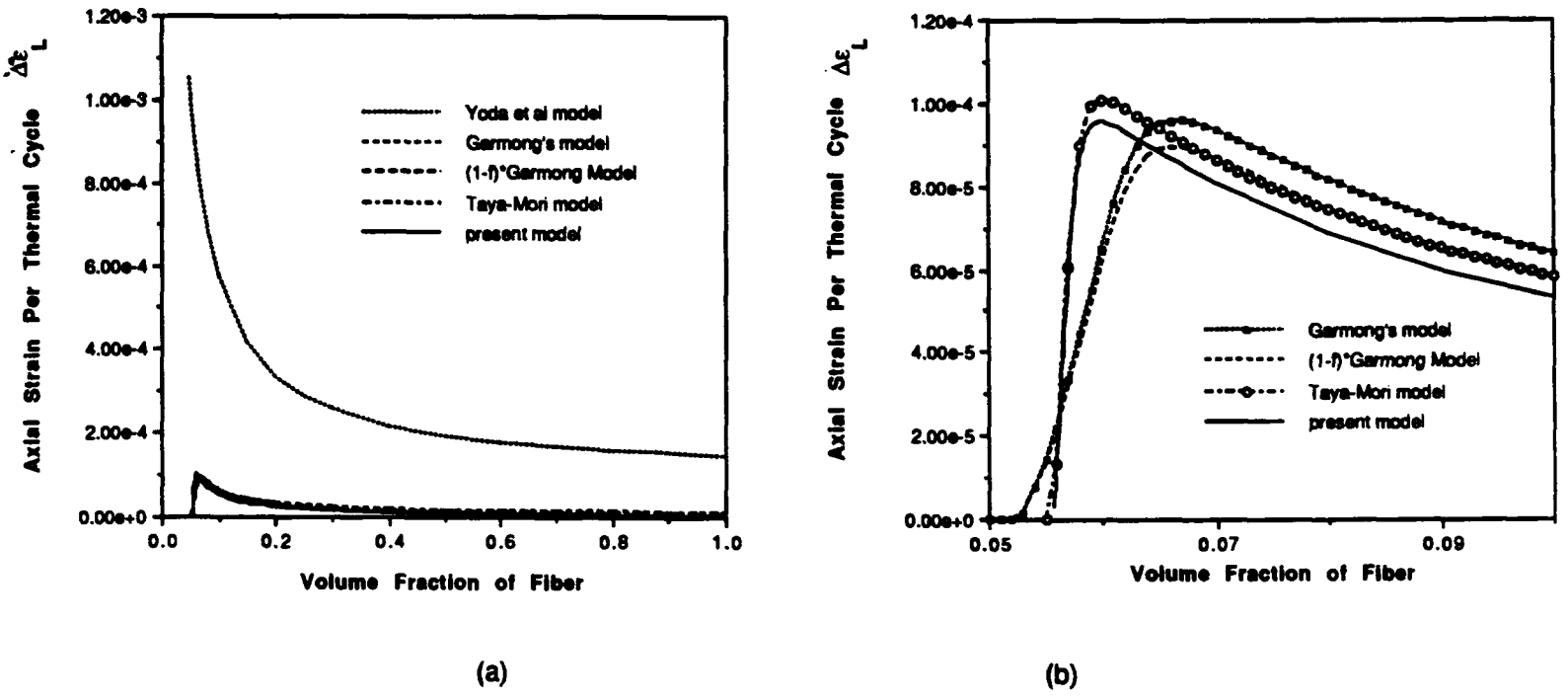

(a) (b)

Figure 16. Comparison of Existing Thermal Cycling Deformation Models with the Present Model, (a) For Entire Range of Volume Fraction, (b) Near the Peak Region.

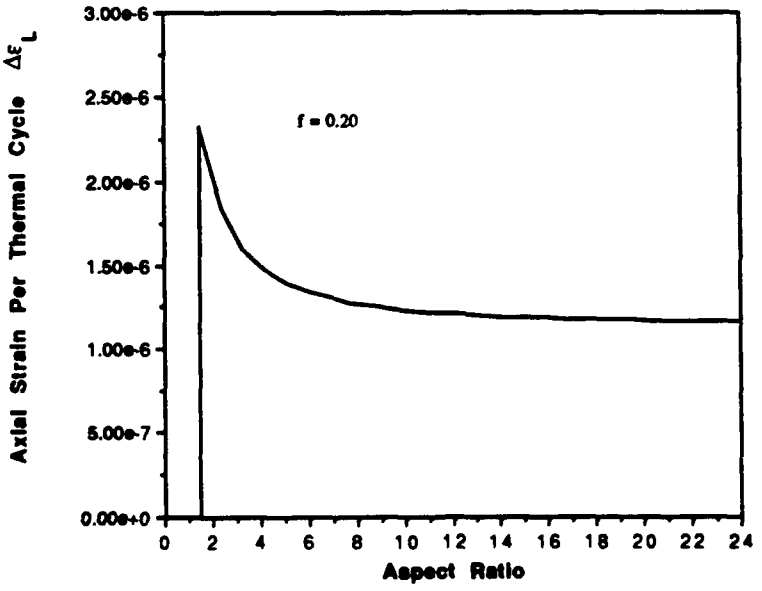

Figure 17. Longitudinal Strain Per Thermal Cycle ($\Delta\varepsilon_L$) Versus Fiber Aspect Ratio for a Volume Fraction 0.20 W-1%ThO_2 Reinforced FeCrAlY Composite.

Table 4. Input-Data for Three MMC Systems

		W-Cu	SiC-Al	W-ThO_2-FeCrYAl
Matrix	E_m(MPa)	1.1×10^{-5}	6.76×10^{4}	2.01×10^{5}
	ν_m	0.35	0.33	0.33
	$\alpha_m(10^{-6}K^{-1})$	20.0	24.7	26.1
	σ_y(MPa)	68.9	50.8	220
	σ_y^{HT}(MPa)	11.4	34.5	6.9
	Creep Constant	1.04×10^{16}	3.41×10^{12}	1.66×10^{25}
	s	4.8	5.08	6.09
Fiber	E_f(MPa)	3.58×10^{5}	4.27×10^{5}	3.58×10^{5}
	ν_f	0.285	0.17	0.285
	$\alpha_f(10^{-6}K^{-1})$	4.75	4.3	4.75
	Aspect Ratio	∞	4.0	5
	f	0.1 and 0.5	0.15	0.2 and 0.3
Thermal Cycle	T_{max}(°C)	800	400	1100
conditions	T_{min}(°C)	200	20	352 and 534
	τ(s)	250	125	260

The prediction based on the present model for the axial dimensional change per cycle $\Delta\varepsilon_L$ of W/Cu composite, shown by a solid curve in Fig. 18, is compared with the experimental results of Yoda et al., resulting in good agreement. In the case of SiCw/Al composite, the SiC whiskers are distributed in-plane with the whisker orientation being semi-random, i.e., not aligned in a specified direction, this represents a departure from the present model, Fig. 13. Hence, the dimensional change per cycle along the transverse direction, $\Delta\varepsilon_T$ is focused on for comparison, for the dimensional change along the thickness direction should not be influenced significantly by the misorientation of fibers. Fig. 19 shows the prediction of $\Delta\varepsilon_T$ by the present model (shown by solid curve) along with the experimental result of Patterson and Taya (filled circle). Again, the present model agrees with the experiment.

In order to apply the present model to the dimensional change along the other directions, one must be given a distribution function of fiber orientation, $\rho(\theta)$ where θ is

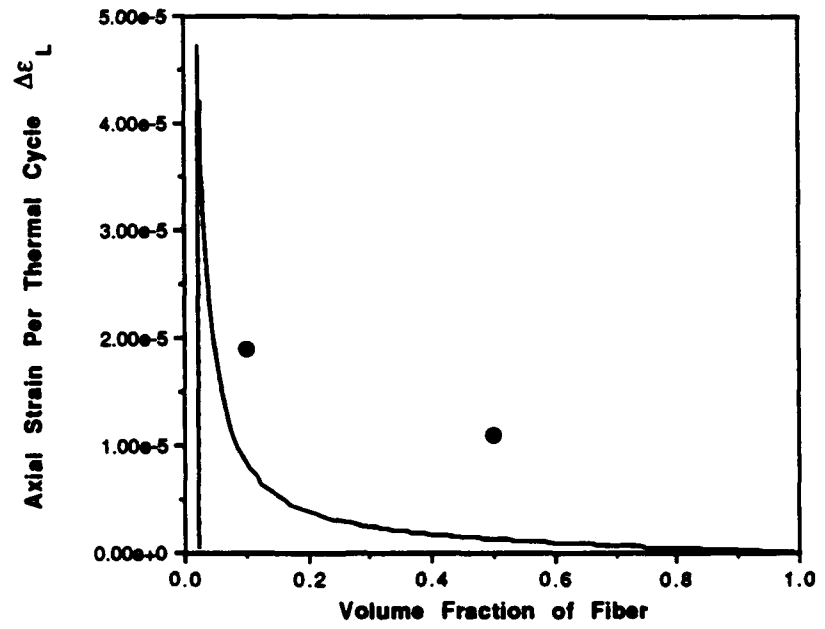

Figure 18. Comparison Between the Prediction of the Present Model and the Experimental Data of Yoda *et al.* for a W-Cu Composite.

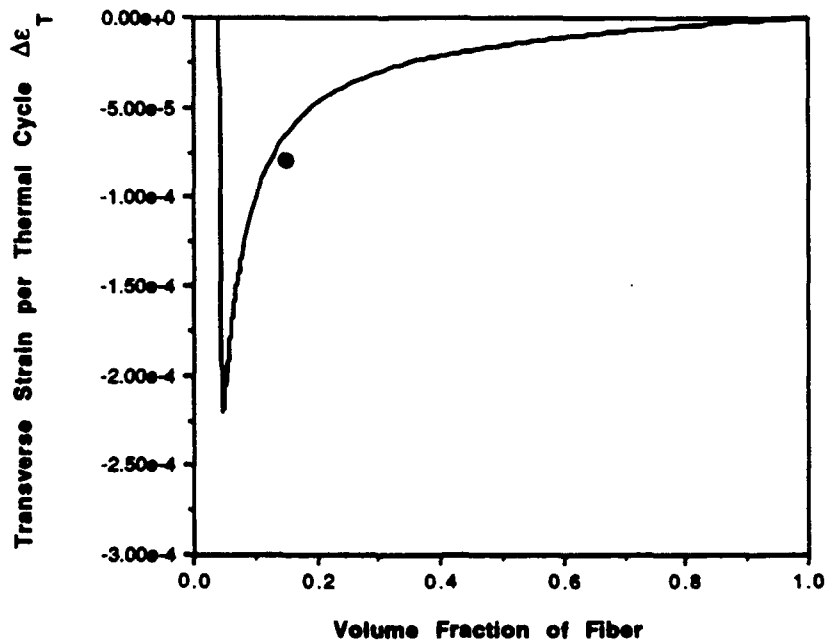

Figure 19. Comparison Between the Prediction of the Present Model and the Experimental Data of Patterson and Taya for a SiC/Al Composite.

the orientation angle of fiber with respect to the reference axis. Taya et al. (26) recently analyzed the dimensional change of a misoriented short fiber composite, the geometry of which is shown in Fig. 20(a) where the distribution function is assumed symmetric with respect to the reference (x_3–) axis, Fig. 20(b). The prediction of accumulated dimensional changes (N = 1000) of a misoriented SiC/Al composite by the model are shown as a function of cut-off angle β (see Fig. 20(b)) in Fig. 21 where the experimental measurements are also shown by the dashed lines. Despite the good agreement between the analytical and experimental results of the through-the-thickness dimensional change (ε_{11}), there exists a poor agreement for the in-plane dimensional changes (ε_{22} and ε_{33}). Namely, there is no unique value of β for which the predictions of all components of dimensional change agree well with the experiment. This is most likely because the actual distribution of short fibers may not be the assumed in-plane semi-random, and the symmetrical distribution of short fibers about the reference axis (x_3-axis) may not be realized in the SiCw/Al composite. In fact, the distribution function could be dependent of both θ and the spherical polar angle φ; i.e. a more general distribution in three-dimensional space. It should be noted in Fig. 21 that for $\beta = \pi/2$, short fibers are distributed in an in-plane completely random manner for which both components of the in-plane dimensional change coincides, i.e. $\varepsilon_{22} = \varepsilon_{33}$.

4.2 Dimensional Change for the Second Stage

Regarding the second stage of dimensional change, an attempt is made to compare the predictions based on our analytical model for progressively debonded interfaces and to limited experimental data.[6,28]

Figure 22 shows a comparison between the progressively debonded interface model and experimental results for the W-1%ThO_2 Fe-25Cr-8Al-0.5Y composite of Fig. 9.[28] The experimental results were obtained for two composite (f = .2) and two monolithic Fe-25Cr-8Al-0.5Y (f = 0) specimens. Here, Δf_N is initially equal to zero but increases by a constant 0.0000025 per thermal cycle, while δf_N remains a constant 0.00002 per thermal cycle. Therefore, after 600 thermal cycles the difference in effective fiber volume fraction between the cooling process and the heating process has increased to 0.0015, and the cooling process effective fiber volume fraction has decreased from an initial value of

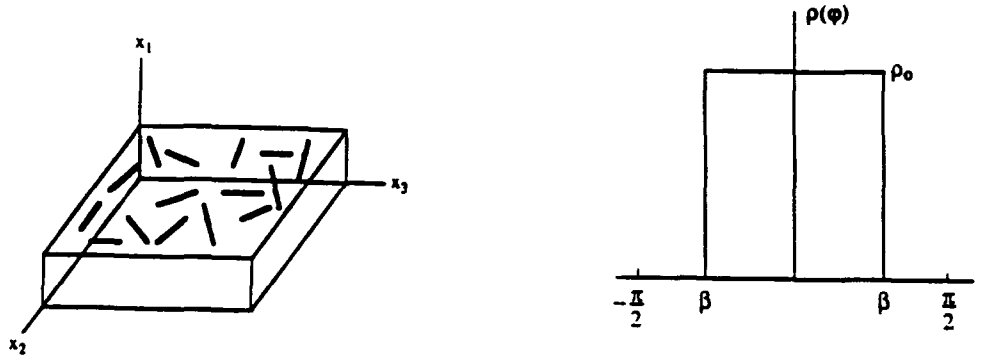

(a) (b)

Figure 20. (a) Misoriented Short Fiber Composite, Where the Misorientation Is In the x_2-x_3 Plane. (b) Uniform Distribution Density Function $\rho(\varphi)$ Bounded by Cut-Off Angle β.

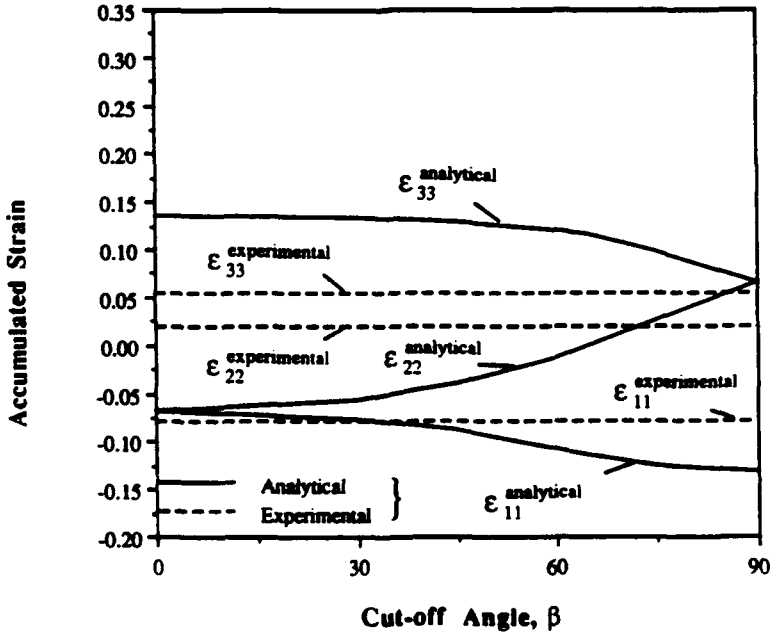

Figure 21. Analytical Results of the Present Model for the Dimensional Change of a SiC-Al Composite After 1000 cycles, Experimental Data of Patterson and Taya are also shown for Comparison.

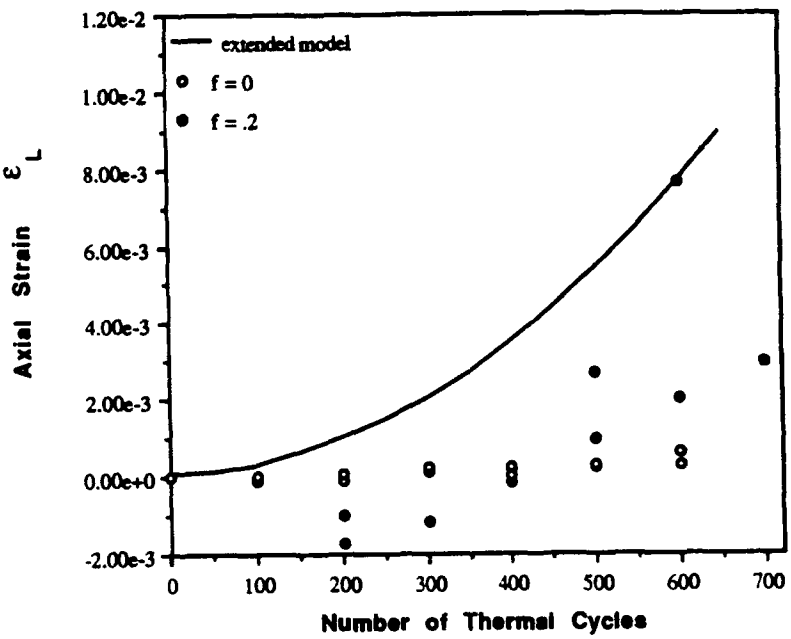

Figure 22. Comparison of analytical predictions of the extended model to experimental results for of the W-1%ThO_2 Fe-25Cr-8Al-0.5Y composite of Fig. 6.

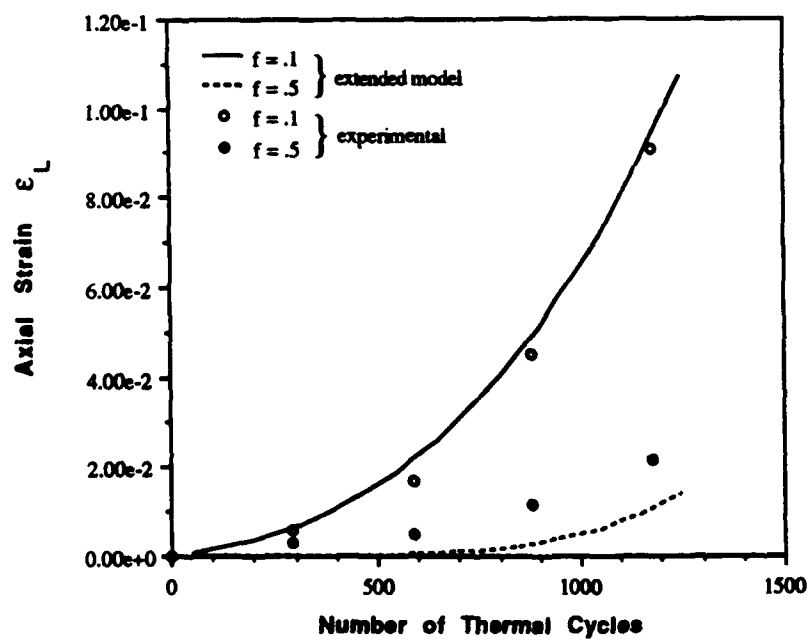

Figure 23. Comparison of analytical predictions of the extended model to the experimental results of Yoda et al. (1978) for a large number of thermal cycles.

0.200 to 0.188. Both of the effective fiber volume fraction quantifications seem within reason given the damage porosity exhibited in Fig. 9. The analytical prediction shown in Fig. 9 assumed that damage development began with the onset of thermal cycling. Better agreement between the analytical predictions and experimental results would exist, however, if damage development was assumed to begin after a critical number of thermal cycles. Additionally, the model does not explain the anomalous compressive strains measured at low numbers of thermal cycles. The model does however, correctly predict that the strain accumulated per thermal cycle becomes much larger as the interfacial damage exhibited in Fig. 9 becomes severe.

Figure 23 shows a similar comparison between the extended model predictions and experimental results for the W-Cu composite system.[6] The basic material property and thermal cycle parameter inputs are the same as that given in Table 4. For the 0.10 initial fiber volume fraction case, Δf_N was initially equal to zero but increased at a constant 0.000005 per thermal cycle, while δf_N remained a constant 0.00002 per thermal cycle. Therefore, after 1000 thermal cycles the difference in effective fiber volume fraction between the cooling process and the heating process had increased to 0.005, and the cooling process effective fiber volume fraction had decreased to 0.08. Both effective fiber volume fraction quantifications seem within reason given the damage porosity discussed by Yoda.[7] In the 0.50 initial fiber volume fraction case, Δf_N was also initially equal to zero but increased at a constant 0.00006 per thermal cycle, while δf_N was a constant 0.00015 per thermal cycle. Figure 9 shows that the correlation between the model results and experimental measurements is very good in the 0.10 initial fiber volume fraction case, however the experimental result in the 0.50 initial fiber volume fraction case is larger than that of the model.

5. CONCLUSIONS

A new thermal cycling strain accumulation model was developed from the previously existing Taya-Mori model (25) which gives quantitative predictions for the strain accumulated per thermal cycle in the case of an aligned fiber reinforced metal matrix composite with perfect interfacial bonding. The present model considered an initially stress free elastic/plastic/creep matrix reinforced with purely elastic, aligned fibers

subjected to an idealized thermal cycle. The present model was found to give results similar to the existing Garmong (24) and Taya-Mori (25) models for the specialized case of continuous fiber reinforced MMCs thermal cycled to a maximum temperature at which creep processes are rapid. The present model is, however, expected to give predictions different from the existing models in the case of a composite with small fiber aspect ratio thermal cycled to a maximum temperature where creep processes are not rapid. The predictions of the model were compared to experimental measurements of the W-Cu material system and the agreement was found to be good. The extension of the basic model to the case of misoriented fiber reinforcement was described, and compared to experiment. Experimental observations of interfacial damage development were exhibited, and these observations were used to formulate a progressive interfacial damage development process in which interfacial damage first occurs near the fiber end at a location of maximum cyclic shear strain. Once initiated, the damage porosity quickly extends towards the fiber longitudinal center. The results of the extended model show that the strain accumulated per thermal cycle dramatically increased from that of the perfectly bonded case, and furthermore, the strain accumulated per thermal cycle increases as the interfacial damage progresses. Thus, the qualitative performance of the extended model agreed with experimental strain measurements of thermal cycled metal matrix composite systems.

Based on the results of the present study, the future research that remains to be conducted is suggested, as described in Appendix B.

6. List of Publications during this Period (1991).

1. J. Echigoya, M. Taya, and W.D. Armstrong, "Thermal Cycling Damage of W-ThO_2 Fiber/FeCrAlY Composite," *Mater. Sci., Eng.,* Vol. A141, 1991, p. 63-66.

2. M. Taya, and W.D. Armstrong, M. Dunn, and T. Mori, "Analytical Modeling of Dimensional Change of Thermally Cycled Metal Matrix Composites," *Mater. Sci. Eng.,* Vol. A143, 1991, p. 143-154.

3. W.D. Armstrong and M. Taya, "Design of a New Creep-Thermal Cycler for High Temperature Metal Matrix Composites," *Experimental Technique,* July/August 1991, p. 33-37.

4. W.D. Armstrong, M. Taya, and M. Dunn, "Strain Accumulation in Thermal Cycled Metal Matrix Composites," ASME Bound Volume, *Damage and Oxidation Protection in High*

Temperature Composites, Vol. II, Metal and Ceramic Matrix, Aerospace/Applied Mechanics Division, Edited by G. K. Haritos and O. O. Ochoa, 1991, p. 51.

5. W.D. Armstrong, M. Ramulu, and M. Taya, "Fabrication of W-1% Reinforced Fe-25Cr-8Al-0.5Y Superalloy Matrix Composite," ASME Bound Volume, *Processing and Fabrication of Composite Materials,*" ASME WAM 1991,Edited by T. S. Srivatsan and S. Chandrashekhar, 1991, p. 291.

REFERENCES

1. M. Taya and R.J. Arsenault: *Metal Matrix Composites: Thermo-mechanical Behavior,* Pergamon Press, Oxford 1989.

2. M.A. Wright: *Metall. Trans.,* 1973, Vol. 6A, p. 129.

3. W.D. Brentnall, D.J. Moracz and I.J. Toth, *Metal Matrix Composites for High Temperature Turbine Blades,* TRW-ER-7722-F, 1975.

4. G.C. Olsen and S.S. Tompkins: *Failure Modes in Composites IV,* TMS-AIME, 1977, p. 1.

5. H.H. Grimes, R.A. Lad and J.E. Maisel: *Metall. Trans.,* 1977, Vol. 8A, p. 1999.

6. S. Yoda, N. Kurihara, K. Wakashima, and S. Umekawa: *Metall. Trans.,* 1978, Vol. 9A, p. 1229.

7. S. Yoda, R. Takahashi, K. Wakashima and S. Umekawa: *Metall. Tarns.,* 1979, Vol. 10A, p. 1796.

8. W.H. Kim, M.J. Koczak, and A Lawley: *New Development and Application in Composites,* D. Kuhlman-Wilsdorf and W.C. Harrigan, Jr. eds., TMS-AIME, 1979, p. 40.

9. D.W. Petrasek and R.A. Signorelli: *Ceramic Eng. Sci. Proc.,* 1981, July-Aug. Amer. Ceram. Soc. 1981, p. 739.

10. R. Warren, L.O.K. Larsson, P. Ekström and T. Jansson: *Progress in Sci. Eng. Composites,* T. Hayashi et al. eds, *J. Soc. Comp. Mater.,* 1982, p. 1419.

11. R.T. Bhatt and H.H. Grimes: *Mech. Prop. Metal Matrix Composites,* J.E. Hack and M.F. Amateux, eds., TMS-AIME, 1983, p. 51.

12. W.G. Patterson and M. Taya: *Proc. Intl. Conf. Comp. Mater.,* W.C. Harrigan, Jr. et al. eds., TMS-AIME, 1985, p. 53.

13. T. Kyono, I.W. Hall and M. Taya: *J. Mater. Sci.,* 1986, Vol. 21, p. 1879.

14. R.C. Wetherhold and L.J. Westfall: *J. Mater. Sci.,* 1988, Vol. 23, p. 713.

15. T. Morimoto and M. Taya: Proc. *Intl. Conf. Fract.-7,* 1989.

16. R. Warren, L.O.K. Larsson, P. Ekstron, Ano T. Jansson, "Progress in Science and Engineering of Composites," Japan Society for Composite Materials, 1982, p. 1419-1426.

17. S.S. Manson: *Thermal Stress and Low Cycle Fatigue,* McGraw-Hill, 1966, p. 246.

18. M. Taya, M. Ramulu, W.D. Armstrong, and M. Dunn, "Damage Accumulation in Advanced Metal Matrix Composites Under Thermal Cycling," Final Report to AFOSR (#89-0059), Feb. 1991. University of Washington, Department of Mechanical Engineering.

19. J. Echigoya, M. Taya, and W.D. Armstrong: *Mater. Sci Eng. A Letters,* Vol. A141, 1991, p. 63.

20. M. Taya and M. Mori, "Dislocations Punched-Out Around a Short Fiber in a Short Fiber Metal Matrix Composite," *Acta Metall.,* Vol. 35, 1987, p. 155.

21. H.A. Saller, J.T. Stacey, and N.S. Eddy: "Investigation of Wrought Iron-Chromium-Aluminum Alloys for Service at 2200°F," Battelle Memorial Institute, #922, 1954.

22. A.K. Mukherjee, J.E. Bird, and J.E. Dorn: *Trans. ASM,* 1969, Vol. 62, p. 155.

23. Y. Takao and M. Taya: *J. Appl. Mech.* Vol. 52, 1985, p. 806.

24. G. Garmong: *Metall, Trans.,* 1974, Vol. 5, p. 2183.

25. M. Taya and T. Mori: *IUTAM Symp. Thermo-mechanical Couplings of Solids,* H.D. Bui and Q.S. Nguyen, eds., Elsevier Sci. Pub., 1987, p. 147.

26. M. Taya , W.D. Armstrong, and M. Dunn, *Material Science Engr.* Vol. A143, 1991, p. 143.

27. W.R. Tyson, *Metall. Trans.*, Vol. 6A, 1975, p. 1674.

28. W.D. Armstrong, M. Taya, and M. Dunn, "Strain Accumulation in Thermal Cycled Metal Matrix Composites," ASME Bound Volume, *Damage and Oxidation Protection in High Temperature Composites,* Vol. II, Metal and Ceramic Matrix, Aerospace/Applied Mechanics Division, Edited by G. K. Haritos and O. O. Ochoa, 1991, p. 51.

Appendix A: Eshelby's Equivalent Inclusion Method

Here we consider a composite which consists of aligned ellipsoidal inhomogeneities Ω with a prescribed eigenstrain $\underset{\sim}{e}^T$ (called an inhomogeneous inclusion) embedded in an infinite matrix, Fig. A(a). The stiffness tensors of the inhomogeneity (fiber) and matrix are denoted by $\underset{\sim}{C}_f$ and $\underset{\sim}{C}_m$, respectively. Consider an arbitrary area in the matrix of the composite where the average disturbance of the stress, ${}^a\underset{\sim}{\sigma}^0_m$ and strain $\bar{\underset{\sim}{e}}$ are related to each other by:

$$ {}^a\underset{\sim}{\sigma}^0_m = \underset{\sim}{C}_m \cdot \bar{\underset{\sim}{e}} \tag{A1} $$

Then introduce an additional inhomogeneous inlusion (fiber) into the average matrix area. The local stress ($\underset{\sim}{\sigma}$) and strain ($\underset{\sim}{e}$) disturbance induced by the introduction of the additional fiber is given by

$$ \begin{aligned} \underset{\sim}{\sigma} &= \underset{\sim}{C}_f \cdot (\bar{\underset{\sim}{e}} + \underset{\sim}{e} - \underset{\sim}{e}^T) \\ &= \underset{\sim}{C}_m \cdot (\bar{\underset{\sim}{e}} + \underset{\sim}{e} - \underset{\sim}{e}^*) \end{aligned} \tag{A2} $$

where $\underset{\sim}{e}^*$ is the presently unknown eigenstrain fictitiously introduced in the fiber domain (Ω), which vanishes outside Ω, and $\underset{\sim}{e}$ is related to $\underset{\sim}{e}^*$ by Eshelby's tensor $\underset{\sim}{S}$

$$ \bar{\underset{\sim}{e}} = \underset{\sim}{S} \cdot \underset{\sim}{e}^* \tag{A3} $$

Equation (A2) indicates that the problem of Fig. A(a) can be converted to that of Fig. A(b). The local stress $\underset{\sim}{\sigma}$ defined by eq. (A2) can represent the internal stress field associated with any fiber (such as the existing one). The volume integral of the internal stress (local stress) over the entire composite domain (D) must vanish:

$$ \int_D \underset{\sim}{\sigma} \, dV = 0 \tag{A4} $$

A substitution of eq. (A2) into (A4) and use of (A1) leads to

$$ \bar{\underset{\sim}{e}} + f(\underset{\sim}{e} - \underset{\sim}{e}^*) = 0 \tag{A5} $$

where f is the volume fraction of fiber. By using eqs. (A3) and (A5), eq. (A2) can be reduced to

$$[(1 - f)\,(\underset{\sim}{C}_f - \underset{\sim}{C}_m) \cdot (\underset{\sim}{S} - \underset{\sim}{I}) + \underset{\sim}{C}_f] \cdot \underset{\sim}{e}^* = \underset{\sim}{C}_f \cdot \underset{\sim}{e}^T \qquad \text{(A6)}$$

Then $\underset{\sim}{e}^*$ is obtained as

$$\underset{\sim}{e}^* = \underset{\sim}{A}^{-1} \cdot \underset{\sim}{C}_f \cdot \underset{\sim}{e}^T \qquad \text{(A7)}$$

where $\underset{\sim}{A}^{-1}$ is the inverse of the 6 x 6 matrix $\underset{\sim}{A}$ defined by

$$\underset{\sim}{A} = (1 - f)\,(\underset{\sim}{C}_f - \underset{\sim}{C}_m) \cdot (\underset{\sim}{S} - \underset{\sim}{I}) + \underset{\sim}{C}_f \qquad \text{(A8)}$$

and where $\underset{\sim}{I}$ is identity matrix.

It is noted in the above calculations that $\underset{\sim}{C}$, $\underset{\sim}{S}$, $\underset{\sim}{I}$ matrices are 6 by 6 while $\underset{\sim}{\sigma}$ and $\underset{\sim}{e}$ are 6 by 1 column vectors.

MT:ldk/dy
11/18/91

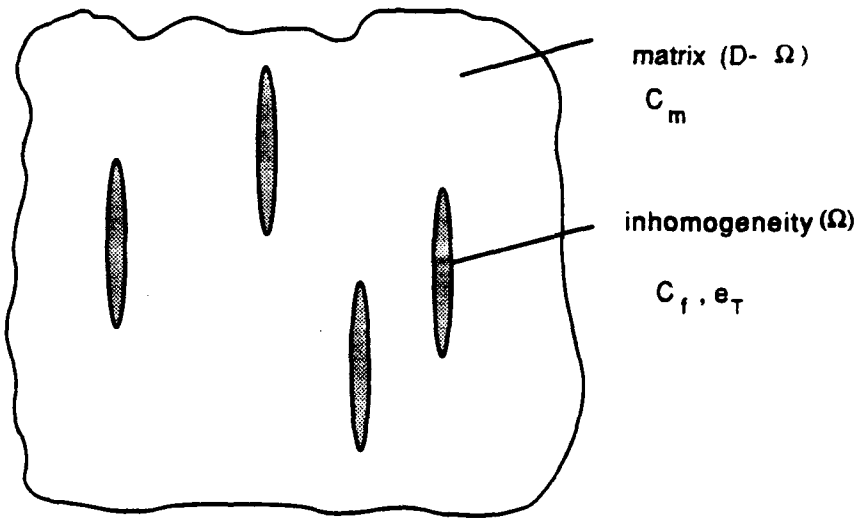

(a)

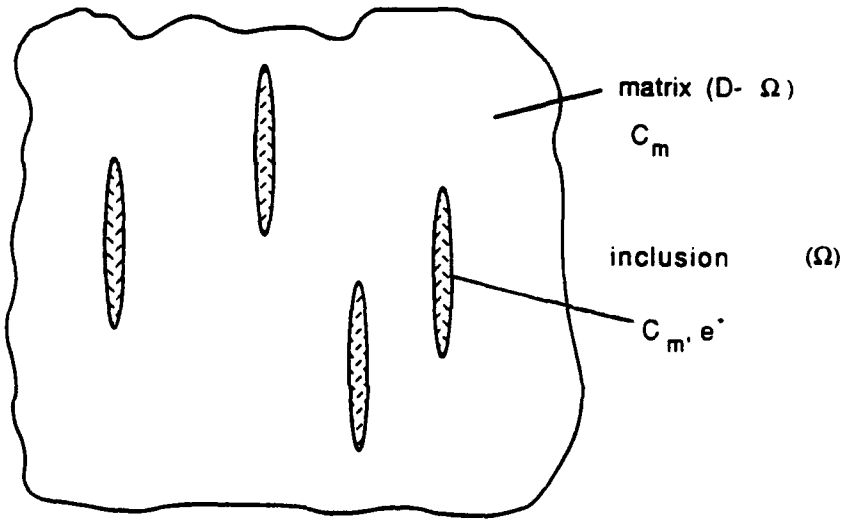

(b)

Fig. A. Eshelby's Model: (a) Inhomogeneity Ω with prescribed eigenstrain e_T, converted to (b) equivalent inclusion Ω with fictitous eigenstrain e^*.

Appendix B: Future Research

The study that remains to be done in the near future is stated in the following:

(1) Document the damage accumulation in W-ThO_2/FeCrAlY composite subjected to combined creep/thermal cycling loadings.

(2) Based on (1), construct a performance map of the composite under creep/thermal cycling loads. An example of such a map is shown in Fig. B.

(3) Apply the present methods of analysis and experimental techniques to Ti-alloy matrix composite system where T_{max} and T_{min} are, respectively, the range of 900°C and –50°C.

As to (2), each iso-damage line indicates a certain degree of damage, for example, 20% reduced stiffness or 10% reduced tensile strength. The intersection points with the vertical axis represent the damage state of MMCs subjected to creep only, whereas those with horizontal line are the damage state induced by thermal cycling only. Hence, the damage state of MMCs induced by combined creep and thermal cycling loads is represented by iso-damage lines between the intersecting points.

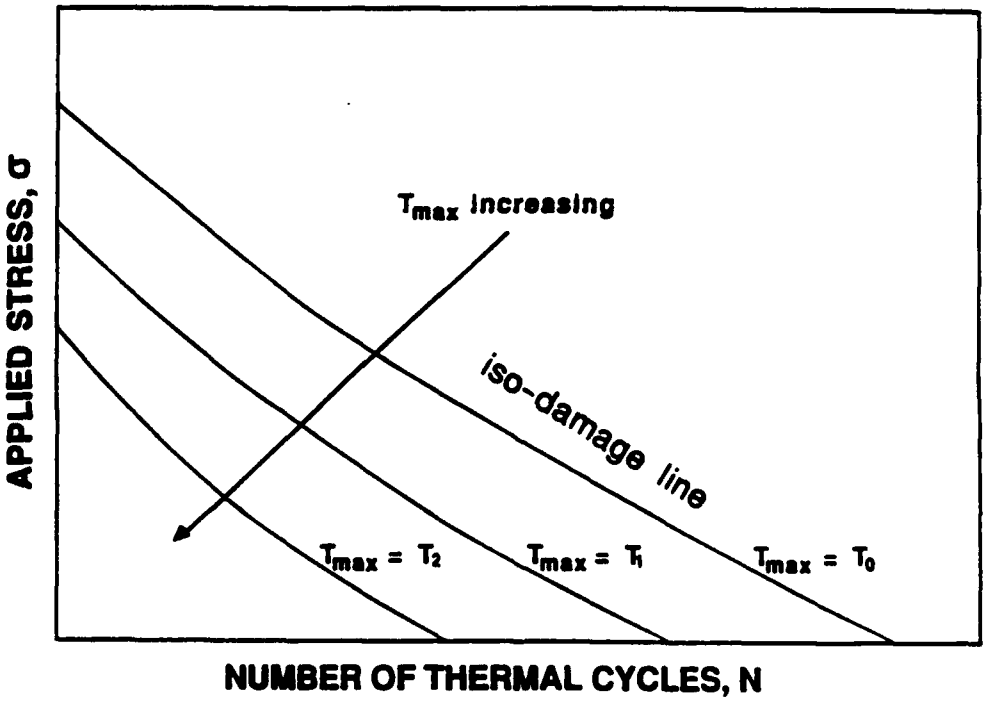

Fig. B. Performance map of an MMC under creep/thermal cycling loadings.

In the case of Ti-alloy matrix composite, its application is most likely to be the skin structure of high speed space vehicles such as NASP or the High Speed Civilian Transport (HSCT). Thus, the appropriate thermal cycling range for Ti-alloy matrix composites would be –50 ~ 900°C. With minor modification of the present apparatus, we can evaluate the thermal cycling resistance of Ti-alloy matrix composite by subjecting it to large numbers of thermal cycling with and without creep loading

MT:ldk
11/14/91